Draft version April 8, 2022
Typeset using LaTeX **twocolumn** style in AASTeX631

Detailed Asteroseismic Modeling of the High-luminosity Red-giant Branch Host Stars KOI-3886 and ι Draconis

Tiago L. Campante [1,2] Tanda Li [3,4,5] J. M. Joel Ong [6] Enrico Corsaro [7] Margarida S. Cunha [1,2] Timothy R. Bedding [8,5] Diego Bossini [1] Sylvain N. Breton [9] Derek L. Buzasi [10] William J. Chaplin [4,5] Morgan Deal [1] Rafael A. García [9] Michelle L. Hill [11] Marc Hon [12,13] Daniel Huber [12] Chen Jiang [14] Stephen R. Kane [11] Cenk Kayhan [15] Jorge Lillo-Box [16] Savita Mathur [17,18] Mário J. P. F. G. Monteiro [1,2] Filipe Pereira [1,2] Nuno C. Santos [1,2] Aldo Serenelli [19,20] and Dennis Stello [13,5]

[1] *Instituto de Astrofísica e Ciências do Espaço, Universidade do Porto, Rua das Estrelas, 4150-762 Porto, Portugal*
[2] *Departamento de Física e Astronomia, Faculdade de Ciências da Universidade do Porto, Rua do Campo Alegre, s/n, 4169-007 Porto, Portugal*
[3] *Department of Astronomy, Beijing Normal University, Beijing, 100875, P. R. China*
[4] *School of Physics and Astronomy, University of Birmingham, Edgbaston, Birmingham B15 2TT, UK*
[5] *Stellar Astrophysics Centre (SAC), Department of Physics and Astronomy, Aarhus University, Ny Munkegade 120, 8000 Aarhus C, Denmark*
[6] *Department of Astronomy, Yale University, 52 Hillhouse Ave., New Haven, CT 06511, USA*
[7] *INAF — Osservatorio Astrofisico di Catania, via S. Sofia 78, 95123 Catania, Italy*
[8] *Sydney Institute for Astronomy (SIfA), School of Physics, University of Sydney, NSW 2006, Australia*
[9] *AIM, CEA, CNRS, Université Paris-Saclay, Université Paris Diderot, Sorbonne Paris Cité, F-91191 Gif-sur-Yvette, France*
[10] *Department of Chemistry and Physics, Florida Gulf Coast University, 10501 FGCU Blvd. S., Fort Myers, FL 33965, USA*
[11] *Department of Earth and Planetary Sciences, University of California Riverside, 900 University Ave., Riverside, CA 92521, USA*
[12] *Institute for Astronomy, University of Hawai'i, 2680 Woodlawn Drive, Honolulu, HI 96822, USA*
[13] *School of Physics, The University of New South Wales, Sydney NSW 2052, Australia*
[14] *Max-Planck-Institut für Sonnensystemforschung, Justus-von-Liebig-Weg 3, 37077 Göttingen, Germany*
[15] *Department of Astronomy and Space Sciences, Erciyes University, 38030, Kayseri, Turkey*
[16] *Centro de Astrobiología (CAB, CSIC-INTA), Depto. de Astrofísica, ESAC Campus 28692 Villanueva de la Cañada (Madrid), Spain*
[17] *Instituto de Astrofísica de Canarias (IAC), E-38205 La Laguna, Tenerife, Spain*
[18] *Universidad de La Laguna (ULL), Departamento de Astrofísica, E-38206 La Laguna, Tenerife, Spain*
[19] *Institute of Space Sciences (ICE, CSIC) Campus UAB, Carrer de Can Magrans, s/n, E-08193, Bellaterra, Spain*
[20] *Institut d'Estudis Espacials de Catalunya (IEEC), Carrer del Gran Capità, 2-4, E-08034, Barcelona, Spain*

ABSTRACT

Asteroseismology is playing an increasingly important role in the characterization of evolved host stars and their planetary systems. Here, we present the detailed asteroseismic modeling of two high-luminosity red-giant branch (HLRGB) hosts, KOI-3886 and ι Draconis, making use of end-of-mission *Kepler* (KOI-3886) and multi-sector TESS (ι Draconis) time-series photometry. This completes a three-article series dedicated to these systems by providing an account of the underlying seismic analyses. We test the impact of adopting different sets of observed modes as seismic constraints. Inclusion of $\ell = 1$ and 2 modes improves the precision, albeit marginally, on the stellar properties compared to radial modes alone, with 1.8–3.0% (radius), 5–9% (mass), and 19–25% (age) reached when using pure π modes as constraints. Given the very small frequency spacing of adjacent dipole mixed modes, the sparse set of observed g-dominated modes is not able to provide extra constraints, resulting in highly multimodal posteriors. Access to multi-year time-series photometry does not improve on the latter, meaning that detailed modeling of HLRGB stars based on (lower-resolution) TESS power spectra

Corresponding author: Tiago L. Campante, Tanda Li, J. M. Joel Ong
tiago.campante@astro.up.pt
litanda@bnu.edu.cn
joel.ong@yale.edu

attains a precision commensurate with that based on end-of-mission *Kepler* data. Furthermore, we test the impact of varying the atmospheric boundary condition. We find mass and radius estimates to be insensitive to the description of the near-surface layers, at the expense of substantially changing both the near-surface structure of the best-fitting models and the values of associated parameters like the initial helium abundance, $Y_{\rm i}$. Attempts to measure $Y_{\rm i}$ from seismic modeling of red giants may thus be systematically dependent on the choice of atmospheric boundary condition.

Keywords: asteroseismology — stars: evolution — stars: fundamental parameters — stars: individual (HD 190655, HD 137759, TYC 3130-2385-1)

1. INTRODUCTION

Throughout the course of the NASA *Kepler*/K2 mission (Borucki et al. 2010; Howell et al. 2014), asteroseismology has played an important role in the characterization of host stars and their planetary systems (for recent reviews, see Campante et al. 2018; Lundkvist et al. 2018). *Kepler*/K2 mainly targeted main-sequence stars, however, observing too few red giants to detect enough planets for robust statistics (Huber et al. 2013; Lillo-Box et al. 2014; Grunblatt et al. 2017, 2019). This meant that the synergy between asteroseismology and exoplanetary science would remain mostly confined to unevolved stars. The advent of NASA's *Transiting Exoplanet Survey Satellite* (TESS; Ricker et al. 2015) has since lifted this restriction, as it enables the systematic search for transiting planets around seismic giants (Campante et al. 2016; Huber et al. 2019; Pereira et al. 2019; Grunblatt et al. 2022; Saunders et al. 2022), as well as revisiting previously known (mostly from radial-velocity surveys) evolved hosts using asteroseismology (Campante et al. 2019; Ball et al. 2020; Jiang et al. 2020; Malla et al. 2020; Nielsen et al. 2020; Kane et al. 2021).

The high-luminosity red-giant branch (HLRGB) host stars KOI-3886 A (HD 190655, KIC 8848288, TIC 185060864; hereafter KOI-3886) and ι Draconis (HD 137759, TIC 165722603; hereafter ι Dra) are paradigmatic cases in this regard (see Table 1 for a compilation of their properties as found in the literature and Fig. 1 for their location on an HR diagram). KOI-3886, observed by *Kepler* for nearly 4 years and later by TESS over 1 sector (27.4 days), has been a longtime candidate host (Rowe et al. 2015). In Lillo-Box et al. (2021), we concluded that the close-in planet candidate is in fact a false positive and reinterpreted the system as an eclipsing brown dwarf in a hierarchical triple containing two evolved stars. The fundamental stellar properties derived from asteroseismology for KOI-3886 (the primary) were central to that work, eventually entering an iterative procedure to determine a final set of properties for the three bodies in the system.

ι Dra, known for two decades to host a planet[1] in a highly eccentric, 511-day-period orbit (Frink et al. 2002; Zechmeister et al. 2008; Kane et al. 2010), was observed by TESS over 5 sectors. In Hill et al. (2021), we presented the results of continued radial-velocity (RV) monitoring of ι Dra over several orbits of its known planet. The newly acquired RV observations allowed us to detect curvature in the previously identified RV trend, which was interpreted as likely being caused by an outer companion. Making use of the precise seismic mass derived for ι Dra, we were able to improve on the precision of planet b's minimum mass. Moreover, through the combination of the RV measurements with space astrometry, we confirmed the presence of an additional long-period, eccentric companion. Mass predictions from our analysis — which used the seismic stellar mass as a prior — place the companion on the border of the planet and brown dwarf regimes.

The presence of planets orbiting KOI-3886 and ι Dra (putative in the former case) is what originally motivated the detailed seismic analyses — conducted separately, although not in a strictly independent manner — of these two K giants. With the present follow-up paper, we complete a *trilogy* dedicated to these systems by providing a full account of the seismic analyses underpinning Lillo-Box et al. (2021) and Hill et al. (2021), placing special emphasis on the detailed asteroseismic modeling of both stars.

Forward modeling of individual mode frequencies (other than radial modes) of HLRGB stars is a state-of-the-art affair (Li et al. 2018; Ong et al. 2021a). Evolutionary calculations in this phase of evolution are particularly sensitive to small variations in the choices of input physics and model parameters, in a highly nonlinear fashion. For instance, small variations in the amount of envelope overshooting result in shifts to both the age and luminosity at which the red-giant luminosity bump

[1] ι Dra b was the first planet found to orbit a giant star (Frink et al. 2002).

occurs, as well as lateral adjustments to the position of the red-giant branch itself on the HR diagram (e.g., Khan et al. 2018). These changes are degenerate with those induced by variations in the mixing-length parameter, $\alpha_{\rm MLT}$, and the initial helium abundance, $Y_{\rm i}$, neither of which can be directly constrained in cool stars. The same is also true of other inputs to stellar evolution, such as the reference values used for solar composition (e.g., Grevesse & Sauval 1998; Asplund et al. 2009), equations of state, or opacity tables, which are not typically treated as variable parameters in grids of stellar models used for this purpose.

To make matters worse, the observational phenomenology for these evolved oscillators requires the involvement of both the usual acoustic waves in the convective stellar exterior, as well as buoyancy waves confined to the stellar interior, in order to fully describe the observed normal modes, which possess mixed p- (or pressure) and g-mode (or gravity) character (e.g., Aizenman et al. 1977; Unno et al. 1989). The treatment of these mixed modes is a numerically sensitive affair (Christensen-Dalsgaard et al. 2020), and the use of mixed modes in stellar modeling itself involves both great computational expense (Ong et al. 2021b) and theoretical sophistication. While modes of quadrupole or higher degree in these red giants may be treated as purely acoustic waves to a good approximation (e.g., Ball et al. 2018), the use of such a prescription for the dipole modes, which are an order of magnitude more strongly mixed (Ong et al. 2021a), is largely untested.

Herein, we test the impact of the optimization procedure by conducting detailed asteroseismic modeling based on three alternative approaches, namely, by using the full mode frequency lists (which include g-dominated modes), pure π modes alone (i.e., adopting the most p-dominated mixed modes), and only considering radial modes. Furthermore, we test the impact of varying the input physics, namely, the treatment of the model atmosphere, on the inferred fundamental stellar properties. This work hence constitutes a valuable incursion into the problematic of detailed asteroseismic modeling of HLRGB stars, for which we make use of high-quality, end-of-mission *Kepler* (KOI-3886) and multi-sector TESS (ι Dra) time-series photometry.

The rest of this paper is organized as follows. In Sect. 2, we present the adopted *Kepler* and TESS photometry. This is followed in Sect. 3 by the analysis of both data sets, including the measurement of individual mode frequencies. Detailed asteroseismic modeling is performed in Sect. 4. Finally, a summary and conclusions are presented in Sect. 5.

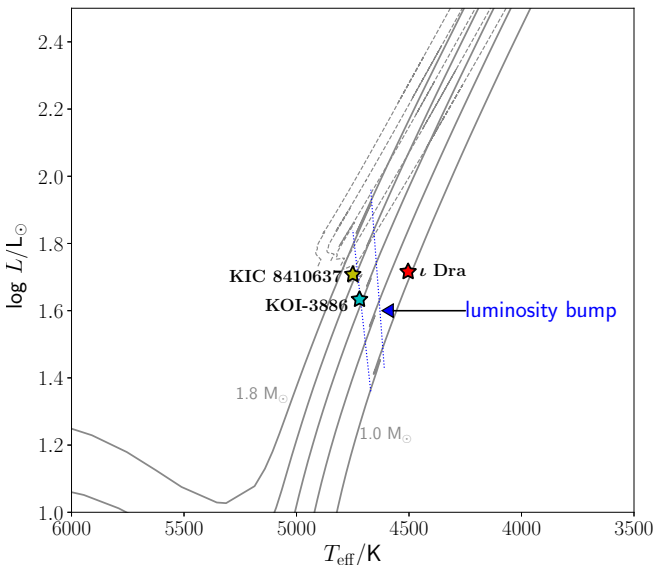

Figure 1. Location of KOI-3886 and ι Dra on an HR diagram. The benchmark star KIC 8410637 (see Sect. 4) is also displayed. Stellar evolutionary tracks (Bossini et al. 2015) ranging in mass from 1.0 to 1.8 $M_\odot$ (in steps of 0.2 $M_\odot$) are shown as solid curves while on the red-giant branch. The location of the red-giant luminosity bump across tracks is delimited by the dotted lines.

2. PHOTOMETRY

KOI-3886 was observed by *Kepler* in long-cadence mode (29.4 minutes) between Quarters 0 and 17 (or for nearly 4 years). It would also be later observed by TESS during Sector 14 (27.4 days) at a faster 2-minute cadence. Owing to the much lower precision and shorter temporal coverage of TESS observations, we have nonetheless decided to base the seismic analysis of KOI-3886 solely on the available *Kepler* photometry. We make use of a KEPSEISMIC[2] light curve, which has been optimized for asteroseismology. The light curve was extracted from the target pixel files using a custom aperture and subsequently processed through the KADACS pipeline (*Kepler* Asteroseismic Data Analysis and Calibration Software; García et al. 2011). KADACS corrects for outliers, jumps, and drifts, also filling any gaps shorter than 20 days using in-painting techniques (García et al. 2014; Pires et al. 2015). The light curve was further high-pass filtered using an 80-day triangular smoothing function, after which it underwent an iterative (three iterations) σ-clipping procedure (3σ level) in order to mitigate the impact of the eclipses on the com-

[2] https://archive.stsci.edu/prepds/kepseismic/

Table 1. Stellar properties for KOI-3886, ι Dra, and KIC 8410637.

	KOI-3886		**ι Dra**		**KIC 8410637**[a]	
Parameter	Value	Source	Value	Source	Value	Source
Gaia Photometry and Parallax						
EDR3 ID	2082133182277361152	1	1614731957531452544	1	2105415749007167616	1
G-band Mag.	10.1	1	2.97	1	10.8	1
π (mas)	2.139±0.307	1	32.52±0.14	1	0.839±0.018	1
Spectroscopy						
$T_{\rm eff}$ (K)	4720±120	2	4504±62	3,4	4750±86	5
[Fe/H] (dex)	0.14±0.07	2	0.03±0.08	3,4	0.12±0.08	5
$\log g$ (cgs)	2.54±0.24	2	2.52±0.07	3,4	2.75±0.15	5
Spectral Energy Distribution (SED) / Joint Light and Velocity Curve Analysis						
L ($L_\odot$)	43.3±9.5	2	52.8±2.1	4	$51.2^{+4.0}_{-3.7}$	6
Reference Fundamental Stellar Properties						
M ($M_\odot$)	···	···	···	···	1.56±0.03[c]	6
R ($R_\odot$)	···	···	11.99±0.06[b]	7	10.74±0.11[c]	6
Global Asteroseismology						
$\Delta\nu$ (μHz)	4.60 ± 0.20	8	4.02 ± 0.02	8	4.63±0.01	5
$\nu_{\rm max}$ (μHz)	46.9 ± 0.3	8	38.4 ± 0.5	8	46.3±0.9	5

[a] Benchmark star (see Sect. 4).

[b] From interferometry.

[c] From the dynamical modeling of the eclipsing binary's orbit.

References—(1) Gaia Collaboration et al. (2021), (2) Lillo-Box et al. (2021), (3) Jofré et al. (2015), (4) Hill et al. (2021), (5) Li et al. (2018), (6) Frandsen et al. (2013), (7) Baines et al. (2011), (8) this work.

putation of the power spectrum. Figure 2 (left panel) shows Quarter 9 of the resulting *Kepler* light curve.

ι Dra was observed by TESS during Sectors 15–16 and 22–24 at a 2-minute cadence. The target's high brightness (apparent TESS magnitude of $T = 2.27$) leads to saturation of the central pixels of a stellar image during a 2-second exposure (each TESS camera acquires a new image every 2 s). To deal with the target's saturated nature, a large custom aperture was adopted and a background model applied to account for the spatially-varying background light (full details on the light curve preparation are given in Hill et al. 2021). There is no detection of a transit signal in the full TESS light curve. Figure 2 (right panel) shows Sectors 22–24 of the resulting TESS light curve.

3. ASTEROSEISMOLOGY

3.1. *Global Oscillation Parameters*

Figure 3 shows the power density spectra of KOI-3886 (left panel) and ι Dra (right panel) based on the Lomb–Scargle periodogram (Lomb 1976; Scargle 1982) of the light curves extracted in Sect. 2. These reveal a clear power excess due to solar-like oscillations at ~ 50 μHz and ~ 40 μHz, respectively. We measured the large frequency separation, $\Delta\nu$, and the frequency of maximum oscillation amplitude, $\nu_{\rm max}$, of both stars using a range of well-tested automated methods (e.g., Huber et al. 2009; Mathur et al. 2010; Corsaro & De Ridder 2014; Campante et al. 2017, 2019; Corsaro et al. 2020). Consolidated pairs of values are listed in Table 1 and stem from a single method for each star (for details, see Lillo-Box et al. 2021; Hill et al. 2021), their uncertainties being the corresponding formal uncertainties.

3.2. *Individual Mode Frequencies*

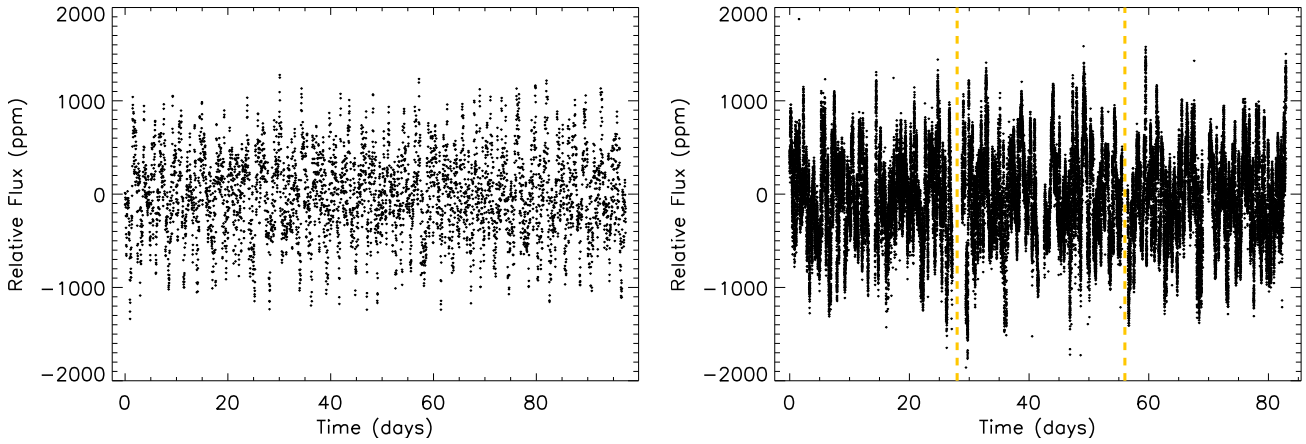

Figure 2. *Left Panel:* Segment of the *Kepler* light curve of KOI-3886 (Quarter 9). The light curve has been resampled onto a regular grid and short gaps filled. *Right Panel:* Segment of the TESS light curve of ι Dra (Sectors 22–24). Vertical dashed lines mark the transition between sectors. Intra-sector gaps are due to the data downlink, separating the two spacecraft orbits in each sector. Note the higher cadence and thus larger density of data points with respect to the *Kepler* light curve.

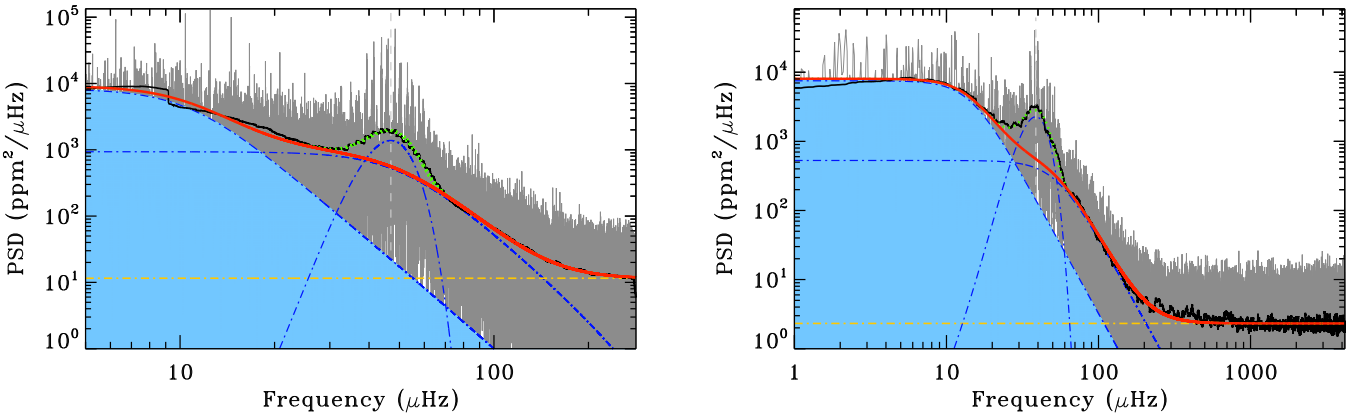

Figure 3. Power spectral density (PSD) of KOI-3886 (left panel) and ι Dra (right panel). Power spectra are shown in gray (heavily smoothed version in black). Vertical dashed lines represent $\nu_{\rm max}$. Solid red curves are fits to the background performed with DIAMONDS (Corsaro & De Ridder 2014), consisting of two Harvey-like profiles (blue dot-dashed curves) and a white noise offset (yellow dot-dashed line). Joint fits to the oscillation power excess (blue dot-dashed Gaussian) and background are visible as green dotted curves near $\nu_{\rm max}$. Note the smaller frequency range of the PSD of KOI-3886, owing to the lower Nyquist frequency of *Kepler*'s long-cadence data. A residual signature of the eclipse harmonics can still be seen at the low-frequency end in the PSD of KOI-3886.

We extracted individual mode frequencies from the power spectrum of each star (a process dubbed *peak-bagging*) using the FAMED pipeline (Fast and AutoMated pEak bagging with DIAMONDS; Corsaro et al. 2020). Tables A1 and A2 list all significant[3,4] modes returned by FAMED for KOI-3886 and ι Dra, respectively. A total of 34 (23) modes of angular degree $\ell = 0$, 1, 2, and 3

[3] A peak is tested against the noise only if its height in the smoothed power spectrum is lower than 10 times the local background level, otherwise it is automatically considered as detected (denoted as '—' in Tables A1 and A2). A detection probability ($p_{\rm det}$) is computed for each low-S/N peak based on a Bayesian model comparison, peaks being deemed significant if $p_{\rm det} \geq 0.993$. See sect. 5.3 of Corsaro et al. (2020) for details.

[4] The Doppler shift of the observed mode frequencies due to the line-of-sight motion (Davies et al. 2014) is not significant for either star and hence no correction has been applied.

were extracted across 8 (7) radial orders for KOI-3886 (ι Dra). Figures A1 and A2 illustrate the outcome of the peak-bagging process.

Owing to the lower resolution of the TESS power spectrum of ι Dra, we have introduced an additional step for selecting mode frequency lists for this star, which combines the output of several peak-bagging procedures. This was mainly motivated by the need to robustly identify and measure long-lived mixed modes. Several *peak-baggers* ($N = 7$) initially extracted individual mode frequencies from the power spectrum of ι Dra. The methods employed included both iterative sine-wave fitting (e.g., Lenz & Breger 2005) as well as the fitting of Lorentzian and sinc^2 mode profiles (e.g., Handberg & Campante 2011), the latter approach being the one implemented in FAMED. Two frequency lists were then produced following the procedure described in Campante et al. (2011), namely, a *maximal frequency list* and a *minimal frequency list*. The former includes modes detected by at least 2 peak-baggers, whereas the latter includes only those modes detected by more than $\lfloor N/2 \rfloor$ peak-baggers. The more conservative minimal list is thus a subset of the maximal list. Importantly, modes in the minimal list are the ones subject to detailed modeling in Sect. 4. To guarantee reproducibility, we resort to a set of observed mode frequencies (and corresponding uncertainties) tracing back to a single method (FAMED), as opposed to an averaged set. We note that Zechmeister et al. (2008), using RV measurements, detected the presence of solar-like oscillations in ι Dra with frequencies around 3–4 d^{-1} ($\sim$ 35–46 μHz), fully consistent with our results. The dominant mode (3.45 d^{-1}) found by those authors coincides with one of the radial modes in the minimal list.

3.3. *Evolutionary State*

Prior knowledge of the evolutionary state of either star is crucial towards an accurate determination of their fundamental properties in Sect. 4. KOI-3886 has been classified in the literature as a hydrogen-shell burning red giant (or RGB) following a number of complementary analyses of its oscillation power spectrum, namely, based on the pressure-mode pattern (Kallinger et al. 2012; Vrard et al. 2018), the morphology of the mixed modes (Elsworth et al. 2017), and deep learning (Hon et al. 2017). The evolutionary state of ι Dra, on the other hand, remains (seismically) unclassified, and we have adopted a number of approaches in this work to address this.

Given the limited number of observed dipole mixed modes per radial order, estimation of the observed period spacing (ΔP; Bedding et al. 2011) of ι Dra based on

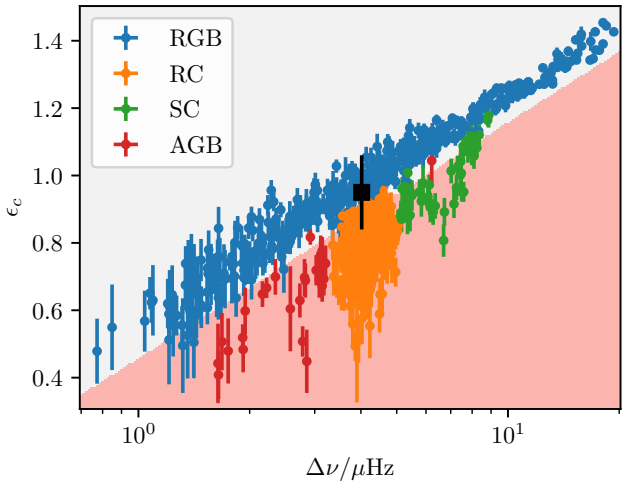

Figure 4. Classification of ι Dra using the p-mode phase offset, ε_c. We show the data set from fig. 4 of Kallinger et al. (2012) as colored points ('RGB' = red-giant branch, 'RC' = red clump, 'SC' = secondary clump, 'AGB' = asymptotic-giant branch) and the measured value of ε_c for ι Dra as the black square. In the background, we show, using shaded regions, the decision boundary of a one-vs-rest support vector machine classifier fitted against the first-ascent red giants of Kallinger et al. (2012). ι Dra lies close enough to the decision boundary that either a first-ascent red giant or red-clump star are plausible descriptions of it.

modes in the minimal list proved unsuccessful. An attempt was then made at constraining the asymptotic period spacing, $\Delta\Pi_1$, based on the stretching of the power spectrum (Vrard et al. 2016), which again was inconclusive. Alternatively, the asymptotic acoustic-mode offset, ε_c, can in principle be used as a discriminant between hydrogen-shell burning (RGB) and helium-core burning (HeB) red giants (Kallinger et al. 2012; Christensen-Dalsgaard et al. 2014). The measured value of $\varepsilon_c = 0.95 \pm 0.11$, however, lies very close (within 1σ) to the decision boundary of Kallinger et al. (2012), potentially allowing for either evolutionary state with this rudimentary method (see Fig. 4).

Machine learning classification methods provided the first robust indication that ι Dra is an RGB star. We ran the time-domain classifier CLUMPINESS (Kuszlewicz et al. 2020) over the full TESS light curve, as well as the two contiguous data subsets, i.e., Sectors 15–16 and Sectors 22–24. The probability of the star being on the RGB is respectively $p = 0.78$, 0.56, and 0.81. The corresponding probability of it being an HeB star is $p = 0.21$, 0.44, and 0.19, with the remaining (negligible) probability being assigned to a *noise* class (e.g., main sequence). Moreover, application of the deep learning classification method of Hon et al. (2017, 2018) to the full TESS light curve, which uses folded background-corrected power

spectra and $\Delta\nu$ as input, gives support to this by favoring an RGB scenario with high confidence ($p > 0.9$).

Finally, we assessed the evolutionary state of ι Dra based on a preliminary grid-based modeling exercise, having considered as observational constraints its global oscillation parameters, $T_{\rm eff}$, [Fe/H], and a parallax-based luminosity (see Table 1). We modeled the star twice, assuming it is either on the RGB or in the red clump (RC). We found that assuming the star to be on the RGB yields a solution fully consistent with the observational constraints as determined by comparing their posterior and input values. On the contrary, if the RC evolutionary state is assumed, the grid-based modeling yields a solution for which the posterior values of the combination $T_{\rm eff}$–[Fe/H] are inconsistent with the input data at the 4σ level (i.e., RC model tracks are unable to simultaneously reproduce the $T_{\rm eff}$ and [Fe/H] constraints). Moreover, if the luminosity constraint is dropped altogether from the analysis, the RC solution then yields $L = 69.5 \pm 3.3\,{\rm L}_\odot$, which is inconsistent with the parallax-based input value of $L = 52.8 \pm 2.1$ L$_\odot$. As a result, the global likelihood of the star being on the RGB is several orders of magnitude higher than it being in the RC. Interpreting this in terms of a Bayes' factor provides decisive evidence in favor of the RGB scenario given the adopted set of seismic and spectroscopic constraints. To test whether this conclusion is robust against the adopted spectroscopic constraints (cf. Campante et al. 2019), we also considered the $T_{\rm eff}$ and [Fe/H] derived from high-resolution optical and near-infrared CARMENES spectra (see table A2 of Marfil et al. 2020), having obtained similar results.

4. DETAILED MODELING

This study makes use of two independent pipelines — hereafter labeled 'TL' and 'JO' — for the detailed modeling. We resort to the TL Pipeline to test the impact of the optimization procedure (Sect. 4.1), investigating how different sets of observed oscillation modes contribute to the characterization of the two HLRGB stars being considered. We next use the JO Pipeline to assess how the choice of model physics, more specifically, the atmospheric boundary condition, modifies the inferred stellar properties (Sect. 4.2). Since the two pipelines employ different underlying grids of stellar models, we are able to roughly characterize the relative importance of these methodological decisions (Sect. 4.3).

Besides KOI-3886 and ι Dra, we also model the benchmark HLRGB star KIC 8410637 (TIC 123417372, TYC 3130-2385-1; Frandsen et al. 2013; Gaulme et al. 2016; Li et al. 2018, 2022; Themeßl et al. 2018), for which multi-year *Kepler* time-series photometry is available. This star was selected both for having a $\nu_{\rm max}$ similar to that of KOI-3886 and ι Dra, as well as for being in an (detached) eclipsing binary. Owing to the latter feature, its mass and radius have been accurately determined via the dynamical modeling of the eclipsing binary's orbit (Frandsen et al. 2013), and can thus provide a direct test to the seismic determination. Observed mode frequencies for KIC 8410637 are taken from table A2 of Li et al. (2018). We also note that a precise (0.5%) interferometric radius is available for ι Dra (Baines et al. 2011), hence providing an additional test. These *reference* fundamental stellar properties are listed in Table 1.

4.1. *Testing the Impact of the Optimization Procedure (TL Pipeline)*

4.1.1. *Stellar Models, Input Physics, and Grid Computation*

We use the stellar evolution code MESA (Modules for Experiments in Stellar Astrophysics, release version 12115; Paxton et al. 2011, 2013, 2015, 2018) and the stellar oscillation code GYRE (v5.1; Townsend & Teitler 2013) to compute a grid of stellar models. We adopt the solar chemical mixture, $(Z/X)_\odot = 0.0181$, provided by Asplund et al. (2009). The MESA ρ–T tables, based on the 2005 update of the OPAL equation of state tables (Rogers & Nayfonov 2002), are adopted and we use OPAL opacities supplemented by the low-temperature opacities from Ferguson et al. (2005). The MESA 'simple' photosphere is used for the set of boundary conditions for modeling the atmosphere, i.e., the opacity of the model atmosphere is specified by the temperature of the outermost mesh point of the interior model via a gray Eddington T–τ relation. The mixing-length theory of convection is applied, parameterized by $\alpha_{\rm MLT}$. We consider convective overshooting in the core, H-burning shell, and envelope. The exponential scheme by Herwig (2000) is applied. The overshoot parameter is mass-dependent and follows the relation $f_{\rm ov} = [0.13\,M(\mathrm{M}_\odot) - 0.098]/9.0$ (Magic et al. 2010). For models with masses above $2.0\,\mathrm{M}_\odot$, we adopt a fixed $f_{\rm ov}$ of 0.018. For a smooth convective boundary, we also apply the MESA predictive mixing scheme. The mass-loss rate on the RGB is characterized by a Reimers' efficiency parameter (Reimers 1975) of $\eta = 0.2$, constrained by seismic targets in the old open clusters NGC 6791 and NGC 6819 (Miglio et al. 2012). Atomic diffusion is only considered for models with masses below $1.1\,\mathrm{M}_\odot$ during the main-sequence phase (it is turned off when the central hydrogen fraction falls below 0.01).

We compute a grid of models with masses ranging from 0.76 to $2.20\,\mathrm{M}_\odot$ and a step size of $0.02\,\mathrm{M}_\odot$. Besides

the stellar mass, M, there are three other independent model inputs, namely, the initial helium fraction, $Y_{\rm i}$, the initial metallicity, $[{\rm Fe/H}]_{\rm i}$, and the mixing-length parameter, $\alpha_{\rm MLT}$. Model input ranges and step sizes are provided in Table 2. We evolve stellar evolutionary tracks from the Hayashi line and terminate them either when $\log g \leq 1.5$ dex on the RGB or helium-core burning starts (corresponding to an increase in the core heavy-element fraction).

4.1.2. *Optimization*

The fitting scheme is based on a maximum likelihood estimation (MLE) approach and is described in detail in Li et al. (2020). We adopt the spectroscopic $T_{\rm eff}$ and [Fe/H] as classical constraints. A luminosity constraint is also adopted, although only in the cases of KOI-3886 and ι Dra. KIC 8410637 is in an eclipsing binary, which can potentially give rise to a biased estimate of the absolute luminosity, that being the reason why we opt for not imposing a luminosity constraint for this star. The fitting scheme employs the two-term surface correction method of Ball & Gizon (2014) and further considers a model systematic uncertainty, which is estimated as the median frequency difference between observations and the best-fitting model. Moreover, mode frequencies are re-weighted as a function of their frequency difference with respect to $\nu_{\rm max}$ when calculating the likelihood.

We test three optimization procedures. The differences between procedures have solely to do with the seismic constraints adopted. The first of these procedures only considers $\ell = 0$ modes; the second includes $\ell = 0$ and 2 modes, as well as the most p-like $\ell = 1$ modes; and the third procedure makes use of all observed mode frequencies (which include g-dominated modes). We refer to these three procedures as methods '0' (radial modes), 'P' (p-dominated modes), and 'A' (all modes), respectively. The most p-like dipole modes are manually selected (cf. Tables A1 and A2). Since these modes are p-dominated, they have relatively high amplitudes and large widths in the power spectrum. Moreover, their frequency pattern on an échelle diagram should exhibit a curvature similar to that of radial modes. We follow both these criteria in manually selecting the most p-like dipole modes.

4.1.3. *Results and Discussion*

Table 3 lists the estimated stellar properties (mass, radius, surface gravity, and age) stemming from each of the three optimization methods. This is complemented by Fig. 5, where the dynamical mass and radius of KIC 8410637, as well as the interferometric radius of ι Dra are also represented. Figure 6 shows the best-fitting models (method 'A') on an échelle diagram as well as the probability distributions (all three methods) for the stellar mass.

We are able to accurately retrieve (i.e., within the quoted measurement uncertainties) the available *reference* stellar properties using each of the optimization methods (see Fig. 5). Inspection of the mass probability distributions (see Fig. 6) further reveals that the estimates returned by the different optimization methods are consistent within 1σ for all three stars (a statement that holds true when applied to the remaining stellar properties, as can be seen in Fig. 5).

The agreement with the dynamical solution for KIC 8410637 is particularly encouraging, especially bearing in mind the systematic overestimation of mass and radius for red giants by asteroseismic scaling relations reported by Gaulme et al. (2016). We applied the scaling relation corrections of Mosser et al. (2013) to all three stars and found, on average, a non-significant overestimation[5] of $\langle \Delta M/M \rangle = 1.6\% \pm 7.0\%$ ($\langle \Delta M/M \rangle = 5.0\% \pm 7.1\%$) and $\langle \Delta R/R \rangle = 2.3\% \pm 3.3\%$ ($\langle \Delta R/R \rangle = 3.2\% \pm 3.3\%$) with respect to the results obtained using method '0' (method 'P'). Although based on a small three-star sample, we nevertheless note that this is in tension with Li et al. (2022), who found a systematic offset of $\sim$ 15% in mass and $\sim$ 7% in radius between the output of the scaling relations and that of detailed modeling (using radial modes) based on a sample of a few thousand RGB stars.

Radial modes alone (method '0') are capable of precisely constraining the stellar properties, reaching a precision of 2.4–3.5%, 6–10%, and 23–28% on the radius, mass, and age, respectively (cf. Li et al. 2022). The inclusion of $\ell = 1$ and 2 modes in the fitting process (methods 'P' and 'A') leads to a marginal gain in precision at best for both KOI-3886 and ι Dra. For KIC 8410637, the extra constraints provided by these modes lead to a more noticeable improvement not only in the precision (e.g., 5.8% on the mass with method 'P' versus 10% with method '0') but also in the accuracy of the stellar property estimates (e.g., a mass accurate within 1.3% with method 'P' versus 7.7% with method '0'). Overall, a precision of 1.8–3.0%, 5–9%, and 19–25% respectively on the radius, mass, and age is attained with method 'P'. We note that these are relatively low-mass stars — eventually igniting helium in the core in degenerate conditions — and thus have core conditions that do not vary significantly. This can be used to explain why the impact of including seismic indicators that probe the core (i.e., $\ell = 1$ g-dominated modes as well as the combi-

[5] In the sense (scaling − modeling)/modeling.

Table 2. Model grids: Input ranges, step sizes, and main differences in terms of the input physics.

Input Parameters	TL Pipeline			JO Pipeline[a]	
	From	To	Step	From	To
M ($M_\odot$)	0.76	2.20	0.02	1.2	2.0
$[Fe/H]_i$ (dex)	−0.5	0.5	0.1	−0.4	0.4
Y_i	0.24	0.32	0.02	0.25	0.32
α_{MLT}	1.7	2.5	0.2	1.55	1.95
Chemical Mixture	Asplund et al. (2009)			Grevesse & Sauval (1998)	
Overshooting	Mass-dependent			None	
Model Atmosphere	'Simple'			Varies	
Surface Correction[b]	Ball & Gizon (2014)			Roxburgh (2016)	

[a] Step sizes undefined as stellar models were computed over a quasirandomly sampled mesh of input parameters.

[b] Concerns the optimization procedure rather than the input physics.

nation of $\ell = 0$ and 2 modes) is limited. This is illustrated, for instance, in figs. 4 and 5 of Lagarde et al. (2016), where the mass dependence of $\Delta\Pi_1$ along the RGB can be seen to almost vanish for $M \lesssim 1.8\,M_\odot$ (see also fig. 4 of Stello et al. 2013). Any residual mass dependence of $\Delta\Pi_1$ thus effectively becomes commensurate with the characteristic uncertainties, i.e., including statistical and systematic[6] contributions, on the observed frequencies for the stars in this study. This explanation holds true except perhaps where the mass approaches the degenerate transition. This is most noticeable in the case of KIC 8410637, for which a luminosity constraint was not imposed, although KOI-3886 also has mass solutions above $1.8\,M_\odot$ that are not removed when including the $\ell = 1$ modes (see Fig. 5).

Moreover, we do not find significant differences between methods 'P' and 'A' in all three cases, i.e., g-dominated dipole mixed modes seem not to provide extra constraints on the inferred stellar properties. By inspecting the mode frequencies of the best-fitting models (see Fig. 6), we notice that these HLRGB stars have very densely spaced dipole mixed modes. At the same time, not every g-dominated mixed mode in the neighborhood of a given p-dominated mixed mode is observed here. If the g-mode (frequency) spacing is sufficiently small, an arbitrary identification of the radial order for each mode may be adopted to fit the dense forest of model g-dominated mode frequencies to the sparse set of observed modes (except perhaps at the highest frequencies, for which the spacing becomes larger than the characteristic uncertainties on the observed frequencies). The resulting posterior distribution for the mass is then highly multimodal (see, e.g., the mass distribution for KOI-3886 corresponding to method 'A' in Fig. 6), with each peak corresponding to a different choice of mode identification (cf. Ong & Basu 2020). This multimodality may in principle be alleviated with an a priori identification of these mixed modes, e.g., through measurement of $\Delta\Pi_1$.

Another aspect worth noting is that the precision achieved on the stellar properties is very similar across the three-star sample. For HLRGB stars, the core becomes increasingly decoupled from the envelope, resulting in surface amplitudes for the g-dominated modes that are too small to make them detectable (see, e.g., Grosjean et al. 2014). Consequently, one ends up with only a few observed g-dominated modes (or a sparse set thereof) per radial order. This is an intrinsic feature and so having access to multi-year time-series photometry (resulting in a high-resolution power spectrum) will not significantly improve on the detailed modeling results for this type of star. For this reason, we obtain similar precision on the stellar properties for the multi-year *Kepler* targets KOI-3886 and KIC 8410637, and the multi-sector TESS target ι Dra, whose temporal coverage is substantially shorter (5 noncontiguous TESS sectors). We tested whether the fact that ι Dra is brighter and closer than the other two stars (see Table 1), thus resulting in more precise non-seismic constraints, could also be an important factor in this regard (cf. Stello et al. 2022). Having artificially degraded the precision on $T_{\rm eff}$ and the luminosity so that they approximately match those for KOI-3886, both methods 'P' and 'A' are able to return similarly precise stellar properties with respect to having adopted the pristine uncertainties. This reinforces our assessment above. We, however, stress that the temporal coverage is still critical for HLRGB stars, as it allows to robustly identify and measure (long-

[6] For reference, the model systematic uncertainty for KIC 8410637, estimated as the median frequency difference between observations and the best-fitting model (cf. Sect. 4.1.2), takes the values 0.012, 0.025, and 0.009 μHz for $\ell = 0$, 1, and 2 modes, respectively.

lived) mixed modes, ultimately determining their reliability (cf. Sect. 3.2).

4.2. *Testing the Impact of the Input Physics: Model Atmosphere (JO Pipeline)*

4.2.1. *Stellar Models, Input Physics, and Grid Computation*

A different set of stellar models was generated with MESA release version 12778 using the relative elemental abundances of Grevesse & Sauval (1998), without element diffusion or convective overshooting, and permitting the initial helium abundances, initial metallicities, and mixing-length parameter to vary freely. A mass-loss rate characterized by a Reimers' efficiency parameter of $\eta = 0.2$ was adopted, as in the previous section. We retained stellar models at a constant temporal spacing of 0.2 Myr, starting from the point where $\nu^2\Delta\Pi_1/\Delta\nu = 5$ (corresponding to roughly $\log g \sim 3.2$) up to core helium exhaustion at the end of the horizontal branch phase of evolution.

Two model grids (grids '1' and '2') were constructed in this manner, although with a different treatment of the model atmosphere. Even if both model grids use photospheric boundary conditions with respect to a gray atmosphere in the Eddington approximation, for grid '1' (or 'spherical atmosphere') the model mesh was extended outwards to an optical depth of $\tau = 10^{-3}$ under spherical geometry (joined with a small plane-parallel section from $\tau = 10^{-4}$ to $\tau = 10^{-3}$), while in grid '2' (or 'plane-parallel atmosphere') the photospheric boundary condition was integrated under plane-parallel geometry from an optical depth of $\tau = 10^{-3}$ to $\tau = \frac{4}{3}$, where it was joined with the inner spherical mesh. The latter boundary condition is the same as that used in the previous section, except that here the atmospheric opacity is allowed to vary consistently with the local temperature and pressure in the atmosphere, rather than being held fixed to the outermost cell of the interior model.

For each choice of input physics, we then computed stellar models over a quasirandomly sampled mesh of initial parameters $\{M, [\mathrm{Fe/H}]_\mathrm{i}, Y_\mathrm{i}, \alpha_\mathrm{MLT}\}$. These values were distributed uniformly over the intervals $M \in [1.2, 2.0]\,\mathrm{M}_\odot$, $[\mathrm{Fe/H}]_\mathrm{i} \in [-0.4, 0.4]$ dex, $Y_\mathrm{i} \in [0.25, 0.32]$, and $\alpha_\mathrm{MLT} \in [1.55, 1.95]$ by sampling over this parameter space with respect to a joint Sobol sequence, 4000 elements long. The initial mass and metallicity were twice as densely sampled as the other parameters, owing to the wide ranges spanned by these parameters.

4.2.2. *Optimization*

For sufficiently evolved red giants ($\Delta\nu \lesssim 5\,\mu$Hz), the uncoupled π-mode frequencies of nonradial modes associated with stellar models may be used in lieu of mixed-mode frequencies to match the most p-dominated observed mixed modes (cf. Ong et al. 2021b), such that the statistical error associated with the mode frequencies still dominates over any systematic errors caused by, e.g., an inappropriate surface-term correction. The numerical evaluation of these π modes is by far computationally cheaper than for mixed modes and, for this reason, we hereafter restrict our attention to these p-dominated modes.

π-mode frequencies (in the sense of Ong & Basu 2020) were computed for $\ell = 0$, 1, and 2 modes within $\pm 4\Delta\nu$ of ν_max. As in Ong et al. (2021a), we applied the ε_ℓ-matching algorithm of Roxburgh (2016) to yield a surface-independent discrepancy function, χ^2_ε, on the internal structure from the mode frequencies. This algorithm operates by constructing diagnostic quantities out of both the model and observed mode frequencies, independently for each degree ℓ. Agreement with the internal structure of the model, insensitive to the stellar surface, is achieved when these quantities collapse to a single function of frequency, in principle minimizing χ^2_ε when a nonparametric functional model is fitted against the data points. In order to permit the inclusion of the dipole modes in this procedure, the most p-like dipole mode was identified manually for each radial order and the associated frequency measurement error was inflated by adding in quadrature the local g-mode spacing, $\nu^2\Delta\Pi_1$, which was also estimated manually. While this mode selection was conducted independently of that in Sect. 4.1.2, almost exactly the same modes ended up being used here (cf. Tables A1 and A2). We chose to use the three lowest-frequency modes (without regard for degree) for the purpose of regularizing the ε_ℓ-matching algorithm, as described in Ong et al. (2021a).

For each model in the grid, we compute a likelihood function, $\mathcal{L} \sim \exp[-\chi^2/2]$, where the discrepancy function, χ^2, is comprised of several terms:

- χ^2_glob, being the sum of error-normalized discrepancies for global properties, namely, the classical spectroscopic quantities T_eff and [Fe/H], the luminosity (adopted only for KOI-3886 and ι Dra; cf. Sect. 4.1.2), and ν_max, computed from models using the scaling relation.

- χ^2_ε, which is the reduced χ^2 statistic returned by the nonparametric ε_ℓ-matching algorithm of Roxburgh (2016).

- χ^2_reg, the regularization term describing the discrepancy for the three lowest-frequency modes. This term is downweighted by a factor of 4, so as

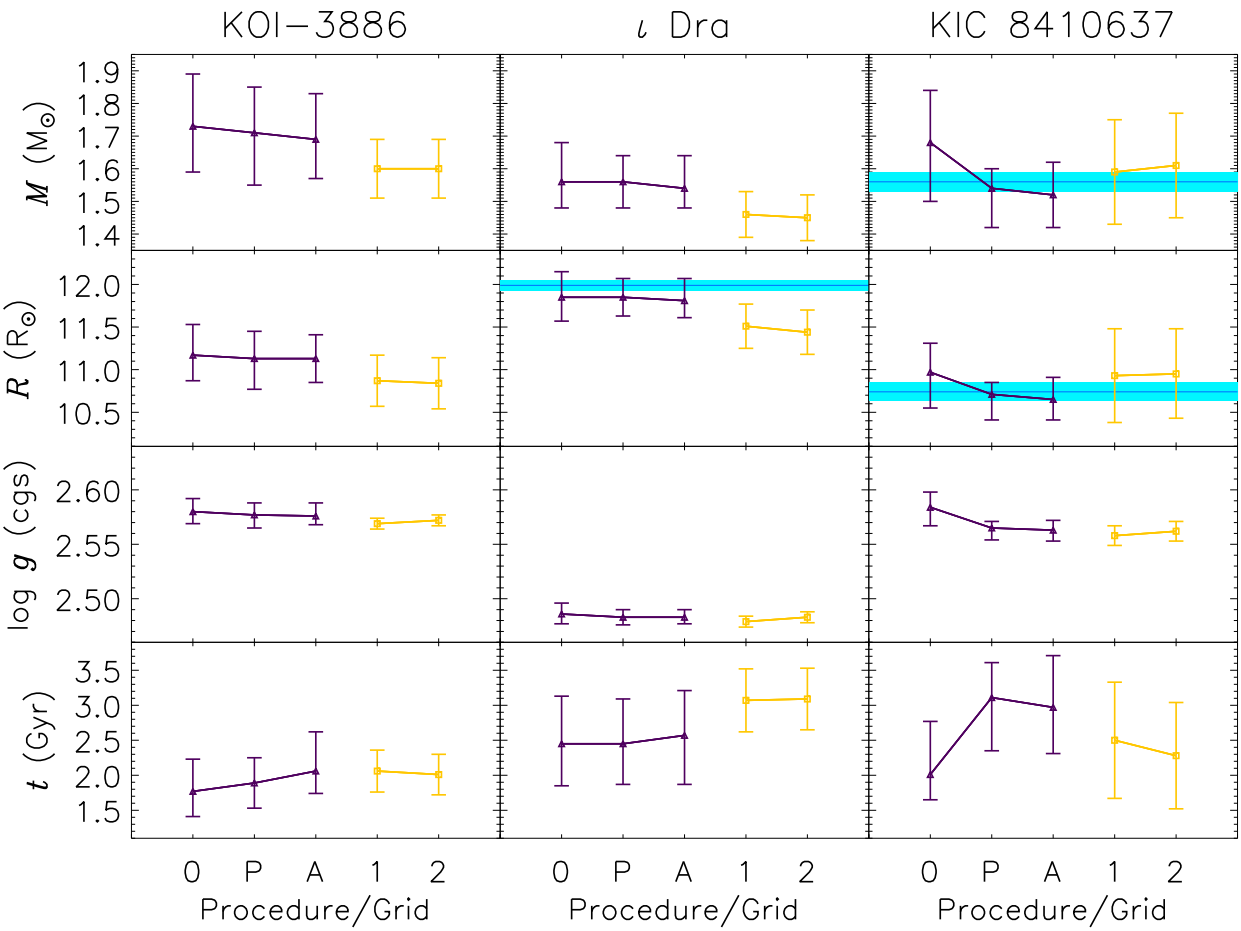

Figure 5. Estimated stellar properties for KOI-3886, ι Dra, and KIC 8410637. Detailed modeling results from the TL (dark purple) and JO (yellow) Pipelines are shown. Procedures/Grids are labeled as '0', 'P', 'A' (cf. Sect. 4.1), and '1', '2' (cf. Sect. 4.2). Blue shaded areas represent the 1σ confidence intervals of the dynamical mass and radius of KIC 8410637, as well as of the interferometric radius of ι Dra.

not to unduly influence the shape of the posterior distribution.

With this likelihood function in hand, we then estimate probability distributions for the stellar properties using the Monte Carlo procedure described in Ong et al. (2021a). In summary, the posterior means for various properties are computed with respect to the likelihood function over the grid of models, normalized by the sampling function of the grid (to impose the assumption of uniform priors). This is done repeatedly with the likelihood function being re-evaluated under randomized perturbations to the observable constraints, as specified by their nominal measurement errors. The resulting distribution of the posterior means is then used to report the values and uncertainties of the desired properties. While it would be prohibitively expensive — computationally speaking — to include perturbations to the mode frequencies, omitting their errors from this procedure has been shown, for main-sequence stars at least, not to appreciably affect the resulting posterior distributions, except that for the stellar age (cf. Cunha et al. 2021). In the case of red giants, however, their rapid evolution is such that their ages and masses are tightly correlated, and so this omission also leads to an underestimation of the uncertainties in properties other than the age. For this reason, we instead report, for each property, the quadratic mean of two different error estimates: the 1σ quantiles of the distribution of the posterior means (the usual approach), as well as the posterior standard deviation associated with a single realization of the procedure (representing the frequency uncertainties).

4.2.3. *Results and Discussion*

We list in Table 4 the mass, radius, surface gravity, and age estimates returned by the above procedure for each star, as applied to the two model grids (see also Fig. 5). As in the previous section, we find very good agreement (i.e., within 1σ) between the results of this

Table 3. Estimated stellar properties for KOI-3886, ι Dra, and KIC 8410637 (TL Pipeline).

Star	M ($M_\odot$)	R ($R_\odot$)	$\log g$ (cgs)	t (Gyr)	Norm. RMS Dev.[a]	Seismic Constraints[b]
KOI-3886	$1.73^{+0.16}_{-0.14}$	$11.17^{+0.36}_{-0.30}$	$2.580^{+0.012}_{-0.011}$	$1.77^{+0.46}_{-0.36}$	0.21 (0.44)	0
	$1.71^{+0.14}_{-0.16}$	$11.13^{+0.32}_{-0.36}$	$2.577^{+0.011}_{-0.012}$	$1.89^{+0.36}_{-0.36}$	0.04 (0.25)	P
	$1.69^{+0.14}_{-0.12}$	$11.13^{+0.28}_{-0.28}$	$2.576^{+0.012}_{-0.008}$	$2.06^{+0.56}_{-0.32}$	0.21 (0.24)	A
ι Dra	$1.56^{+0.12}_{-0.08}$	$11.85^{+0.30}_{-0.28}$	$2.486^{+0.010}_{-0.009}$	$2.45^{+0.68}_{-0.60}$	0.12 (0.45)	0
	$1.56^{+0.08}_{-0.08}$	$11.85^{+0.22}_{-0.22}$	$2.483^{+0.007}_{-0.007}$	$2.45^{+0.64}_{-0.58}$	0.09 (0.51)	P
	$1.54^{+0.10}_{-0.06}$	$11.81^{+0.26}_{-0.20}$	$2.483^{+0.007}_{-0.006}$	$2.57^{+0.64}_{-0.70}$	0.14 (0.33)	A
KIC 8410637	$1.68^{+0.16}_{-0.18}$	$10.97^{+0.34}_{-0.42}$	$2.584^{+0.014}_{-0.017}$	$2.01^{+0.76}_{-0.36}$	0.84 (0.82)	0
	$1.54^{+0.06}_{-0.12}$	$10.71^{+0.14}_{-0.30}$	$2.565^{+0.006}_{-0.011}$	$3.11^{+0.50}_{-0.76}$	0.54 (0.59)	P
	$1.52^{+0.10}_{-0.10}$	$10.65^{+0.26}_{-0.24}$	$2.563^{+0.009}_{-0.010}$	$2.97^{+0.74}_{-0.66}$	0.60 (0.61)	A
					0.31 (0.47)†	

[a] Normalized RMS deviation about the mean ($d_{\rm norm}$; see Eq. 1). Values outside (inside) brackets are computed considering mean property values across the set of procedures '0', 'P', and 'A' (all procedures/grids, i.e., '0', 'P', 'A', '1', and '2'). See Sect. 4.3 for details.

[b] '0': $\ell = 0$ modes only; 'P': $\ell = 0$ and 2 modes, as well as most p-like $\ell = 1$ modes; 'A': All observed modes.

† Average value, i.e., $\langle d_{\rm norm} \rangle$.

exercise and both the dynamical mass and radius of KIC 8410637. The radius for ι Dra is in slight ($\sim 2\sigma$) tension with the interferometric radius from Baines et al. (2011). We note that interferometric angular diameters can be subject to calibration biases (White et al. 2018), in particular for measurements taken over a limited range of baselines or with partially resolved calibrators. Some of the systematic differences in angular diameters between stars observed with different instruments (Tayar et al. 2022) could account for the observed difference with respect to the asteroseismic radius. The Monte Carlo procedure also allows estimating and comparing both the marginal and joint posterior distributions of the stellar properties, which we show in Figs. 7 to 9. Note, following our discussion above, that the widths of the distributions returned by the bootstrapping procedure, which quantify the variations in the posterior mean under different realizations of the random error, are smaller than the reported uncertainties (these also include the posterior variances associated with individual realizations).

In Figs. 7 to 9, results corresponding to each choice of the atmospheric boundary condition are represented by the blue (grid '1' or 'spherical atmosphere') and orange (grid '2' or 'plane-parallel atmosphere') contours and histograms. We see marked differences in some of the inferred stellar properties. In particular, although the estimated masses and radii are not substantially changed relative to the reported uncertainties, the changes in the estimated mean densities (which combine them as $\rho \sim M/R^3$) are larger than the reported uncertainties for both KOI-3886 and ι Dra. This is likely in part because the mean density is constrained (albeit indirectly, via the seismic data) with an order of magnitude more relative precision than either M or R separately. On the other hand, this effect is not seen for KIC 8410637, for which a luminosity constraint was not adopted in this exercise. Since L is not imposed, changing the atmospheric boundary condition may allow the best-fitting model to have potentially a different luminosity (and therefore mass and age) in order to better satisfy the very tight $\Delta\nu$ constraint.

Aside from these statistical considerations, there are also significant physical and methodological implications associated with changing the atmospheric boundary condition. In terms of the spectroscopic observables, it is well-established that the choice of atmospheric boundary condition strongly determines the location of the RGB on the HR diagram associated with any given pair of $Y_{\rm i}$, the initial helium abundance, and $\alpha_{\rm MLT}$, the mixing-length parameter. Accordingly, when the atmospheric boundary condition is changed, the values of $Y_{\rm i}$ and $\alpha_{\rm MLT}$ that produce consistency with a fixed set of temperature and luminosity constraints must also be adjusted. Indeed, we see this happening in the bottom rows of Figs. 7 to 9, which show the joint and

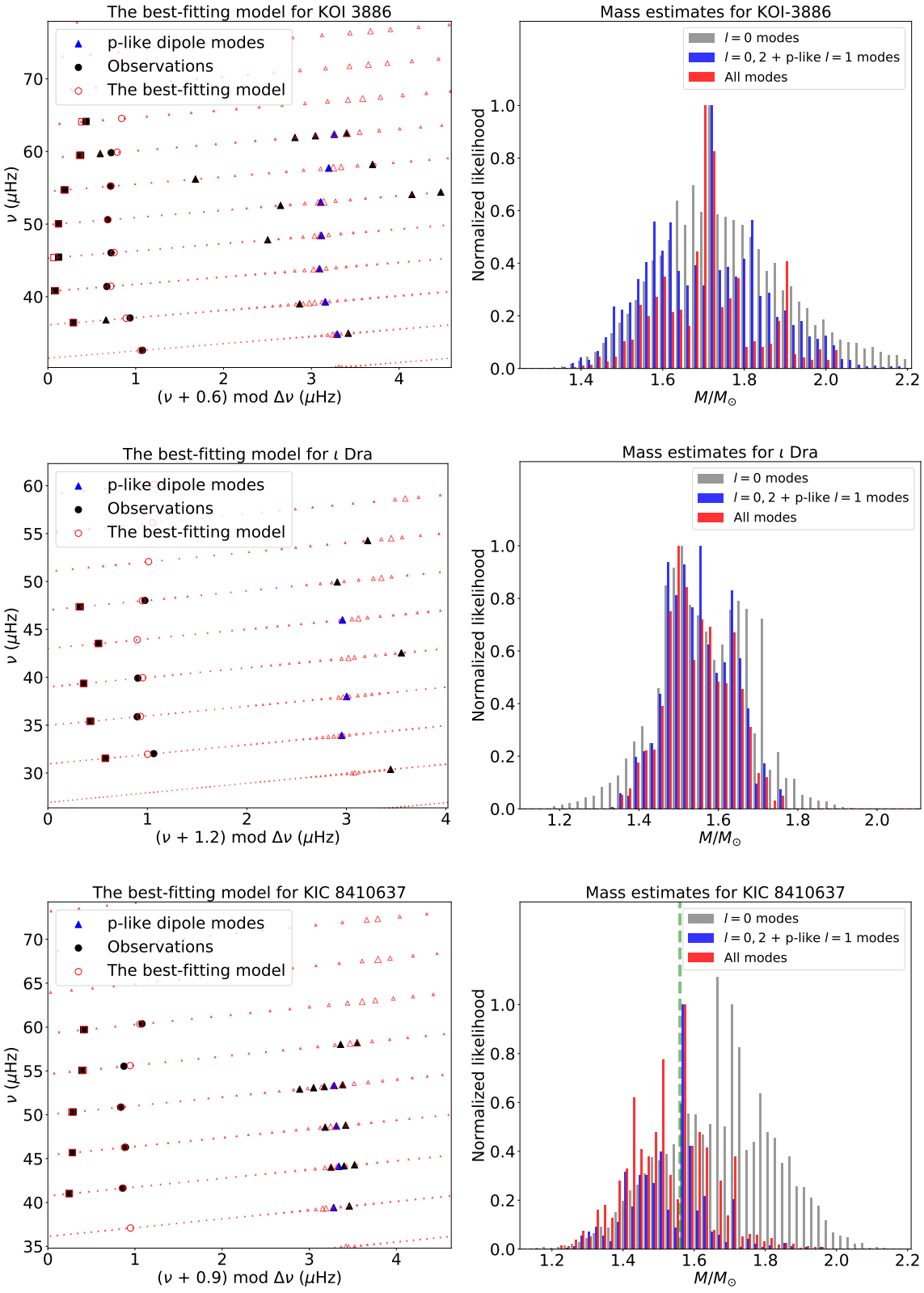

Figure 6. *Left Column:* Échelle diagrams of the best-fitting models for (from top to bottom) KOI-3886, ι Dra, and KIC 8410637 constrained by all the observed mode frequencies (method 'A'). Circles, triangles, and squares represent $\ell = 0$, 1, and 2 modes, respectively (the most p-like dipole modes are rendered in dark blue). A range of mixed $\ell = 1$ model frequencies are plotted with their symbol size scaled by the mode inertia (larger size means that the mode is more p-dominated). *Right Column:* Probability distributions for the stellar mass estimated using each of the three optimization methods ('0' in gray, 'P' in blue, and 'A' in red). The vertical dashed line in the bottom panel represents the dynamical mass of KIC 8410637.

marginal distributions of $Y_{\rm i}$ for each of the three stars, where the value of $Y_{\rm i}$ that best describes each star is significantly modified (this is particularly noticeable in the case of ι Dra) between each choice of atmospheric boundary condition.

Changing the atmospheric boundary condition also modifies the mode frequencies of a stellar model (inducing a numerical seismic surface term). Existing methodological comparisons of surface term treatments for red giants (Ball et al. 2018; Jørgensen et al. 2020; Ong et al. 2021a), or even in general (Basu & Kinnane 2018; Compton et al. 2018; Nsamba et al. 2018), have usually considered the effects of different parameterizations of, or corrections for, modeling errors in stellar surfaces, under numerical experiments in which these modeling errors (arising from how the underlying set of stellar models is being generated) are kept the same. In this case, however, we have performed a converse experiment: We have maintained the use of a single algorithm to mitigate the asteroseismic surface term throughout — the surface-independent ε_ℓ-matching scheme of Roxburgh (2016) — while changing the atmospheric boundary condition associated with the 1D evolutionary models. In particular, we have chosen a mitigation scheme that is designed to yield seismic constraints which are insensitive to the near-surface layers altogether, rather than attempting to correct their effects on the mode frequencies per se. Accordingly, the resulting systematics which we obtain originates from how the spectroscopic, rather than seismic, properties of the stellar models depend on the construction of their surface layers.

We see here that seismic estimates of mass and radius appear methodologically insensitive to the description of these near-surface layers. This occurs at the expense of substantially changing both the near-surface structure of the best-fitting models (i.e., changing the calibration constant in the scaling relation between $\Delta\nu$ and the mean density, which relies on homology arguments) and the values of associated parameters like the initial helium abundance (in tandem with the interaction with the spectroscopic constraints above). This has been illustrated in this work by the atmospheric boundary condition, but other unknown/incomplete contributions of the near-surface physics may have a similar impact. Some alternatives are the modeling of the superadiabatic layer, incorporation of atmospheric convective overshooting, or incorrect atmospheric opacities. This issue implies that attempts to measure $Y_{\rm i}$ from seismic modeling of red giants, e.g., for the purpose of Galactic chemical evolution (measuring $\mathrm{d}Y/\mathrm{d}Z$ relations) or Galactic archaeology studies, are systematically impacted by the modeling of the surface layers.

4.3. *Intra- vs. Inter-pipeline Dispersion*

Since the input physics underlying the TL and JO Pipelines differs in a number of aspects (cf. Table 2), a meaningful investigation of the source(s) of inter-pipeline systematics would not be possible. The exercises carried out in Sects. 4.1 and 4.2 should instead be regarded as independent, i.e., we are interested in assessing the intra- as opposed to the inter-pipeline dispersion.

We find it nonetheless instructive to roughly characterize the relative importance of the methodological choices made when operating each of these pipelines. To that end, we introduce a simple statistic, namely, the normalized root-mean-square (RMS) deviation about the mean:

$$d_{\rm norm} = \sqrt{\frac{1}{4}\sum_i \left(\frac{p_i - \mu_{p_i}}{\sigma_i}\right)^2}\,, \qquad (1)$$

where p_i represents each of the four estimated stellar properties (M, R, $\log g$, and t), σ_i is the associated uncertainty, and μ_{p_i} is the property's mean value across a set of procedures/grids. We compute $d_{\rm norm}$ for each star and procedure/grid combination and list it in Tables 3 and 4. Values outside brackets are computed considering mean property values across the set of procedures/grids within the same pipeline (i.e., TL or JO). Values inside brackets are computed considering mean property values across all procedures/grids (i.e., TL and JO combined). Average values, $\langle d_{\rm norm}\rangle$, are also provided, which can be interpreted as proxies for the intra- and inter-pipeline systematics, respectively. Figure 5 provides a visual aid.

Two features are worth noting. First, the inter-pipeline systematics dominates over the intra-pipeline systematics. This is more noticeable in the case of the JO Pipeline, whose intra-pipeline systematics is a factor of ~ 2 smaller than for the TL Pipeline. Second, the uncertainties on the stellar properties returned by both pipelines are robust in the sense that their magnitudes are larger than the inter-pipeline (and hence intra-pipeline) systematics, i.e., $\langle d_{\rm norm}\rangle < 1$ everywhere.

5. SUMMARY AND CONCLUSIONS

We have conducted detailed asteroseismic modeling of the HLRGB host stars KOI-3886 and ι Dra, making use of two independent pipelines. A third star, KIC 8410637, a member of an eclipsing binary, was also modeled and used as benchmark. Multi-year *Kepler* time-series photometry is available for both KOI-3886 and KIC 8410637, whereas multi-sector TESS time-series photometry is available for ι Dra (ι Dra is, furthermore, a saturated target in the TESS photometry).

Using one of the pipelines (TL Pipeline; Sect. 4.1), we first tested the impact of the optimization procedure

Table 4. Estimated stellar properties for KOI-3886, ι Dra, and KIC 8410637 (JO Pipeline).

Star	M ($M_\odot$)	R ($R_\odot$)	$\log g$ (cgs)	t (Gyr)	Norm. RMS Dev.[a]	Model Grid[b]
KOI-3886	$1.60^{+0.09}_{-0.09}$	$10.87^{+0.30}_{-0.30}$	$2.569^{+0.005}_{-0.005}$	$2.06^{+0.30}_{-0.30}$	0.16 (0.75)	1
	$1.60^{+0.09}_{-0.09}$	$10.84^{+0.30}_{-0.30}$	$2.572^{+0.005}_{-0.005}$	$2.01^{+0.29}_{-0.29}$	0.16 (0.56)	2
ι Dra	$1.46^{+0.07}_{-0.07}$	$11.51^{+0.26}_{-0.26}$	$2.479^{+0.005}_{-0.005}$	$3.07^{+0.45}_{-0.45}$	0.21 (0.75)	1
	$1.45^{+0.07}_{-0.07}$	$11.44^{+0.26}_{-0.26}$	$2.483^{+0.005}_{-0.005}$	$3.09^{+0.44}_{-0.44}$	0.21 (0.78)	2
KIC 8410637	$1.59^{+0.16}_{-0.16}$	$10.93^{+0.55}_{-0.55}$	$2.558^{+0.009}_{-0.009}$	$2.50^{+0.83}_{-0.83}$	0.13 (0.48)	1
	$1.61^{+0.16}_{-0.16}$	$10.95^{+0.53}_{-0.52}$	$2.562^{+0.009}_{-0.009}$	$2.28^{+0.76}_{-0.76}$	0.14 (0.34)	2
					0.17 (0.61)†	

[a] Normalized RMS deviation about the mean ($d_{\rm norm}$; see Eq. 1). Values outside (inside) brackets are computed considering mean property values across grids '1' and '2' (all procedures/grids, i.e., '0', 'P', 'A', '1', and '2'). See Sect. 4.3 for details.

[b] '1': Spherical atmosphere; '2': Plane-parallel atmosphere. See Sect. 4.2.1 for details.

† Average value, i.e., $\langle d_{\rm norm} \rangle$.

by adopting different sets of observed oscillation modes as seismic constraints, namely, radial modes (method '0'), p-dominated modes (method 'P'), and all modes (method 'A'). The main outcomes of this exercise are as follows:

— Radial modes alone (method '0') are capable of accurately and precisely constraining the stellar properties. A precision of 2.4–3.5%, 6–10%, and 23–28% respectively on the radius, mass, and age is thus attained (cf. Li et al. 2022). Inclusion of $\ell = 1$ and 2 modes (methods 'P' and 'A') improves precision only marginally, with 1.8–3.0%, 5–9%, and 19–25% being reached when $\ell = 0$ and 2 modes, as well as the most p-like $\ell = 1$ modes, are used as constraints (i.e., method 'P'). The limited impact of including seismic probes into the core of these relatively low-mass stars ($M \lesssim 1.8\,M_\odot$) can be explained by the fact that their core conditions do not vary significantly, as attested by the vanishing mass dependence of $\Delta\Pi_1$ along the RGB (cf. Stello et al. 2013; Lagarde et al. 2016). However, for masses above this threshold, and limited classical constraints, core seismic constraints can have an impact. This is seen in the case of KIC 8410637, for which a luminosity constraint was not imposed. Here, $\ell = 0$ modes alone produce statistically significant solutions for masses beyond $1.8\,M_\odot$, which are ruled out when the $\ell = 1$ modes are included in the fitting process.

— Given the very small frequency spacing of adjacent dipole mixed modes characteristic of HLRGB stars, the sparse set of observed g-dominated modes is not able to provide extra constraints on the inferred stellar properties. This happens because an arbitrary identification of the radial order for each mode may be adopted to fit the dense forest of model g-dominated mode frequencies, resulting in posterior distributions for the stellar mass that are highly multimodal (cf. Ong & Basu 2020). In principle, this multimodality may be alleviated by supplying an a priori identification for the radial orders of the observed mixed modes. In practice, however, doing so would require both accurate estimation of $\Delta\Pi_\ell$, as well as constraints on allowable values for the g-mode phase function, $\varepsilon_{\rm g}$, near $\nu_{\rm max}$. Such constraints may be provided, for example, by JWKB analysis of the g-mode cavity when the star is significantly more or significantly less evolved than the RGB luminosity bump (Pinçon et al. 2019), or by homology relations in stars with degenerate helium cores given $\Delta\Pi_\ell$ (Deheuvels et al. 2021). However, more general considerations may require further theoretical investigation.

— For the reasons stated above, it is the shorter-lived p-dominated mixed modes that mostly end up constraining the stellar properties of HLRGB stars. Therefore, despite the much shorter temporal coverage (and thus lower resolution of the power spectrum) available for TESS targets compared to multi-year *Kepler* observations, detailed modeling of the former can lead to similarly precise stellar properties.

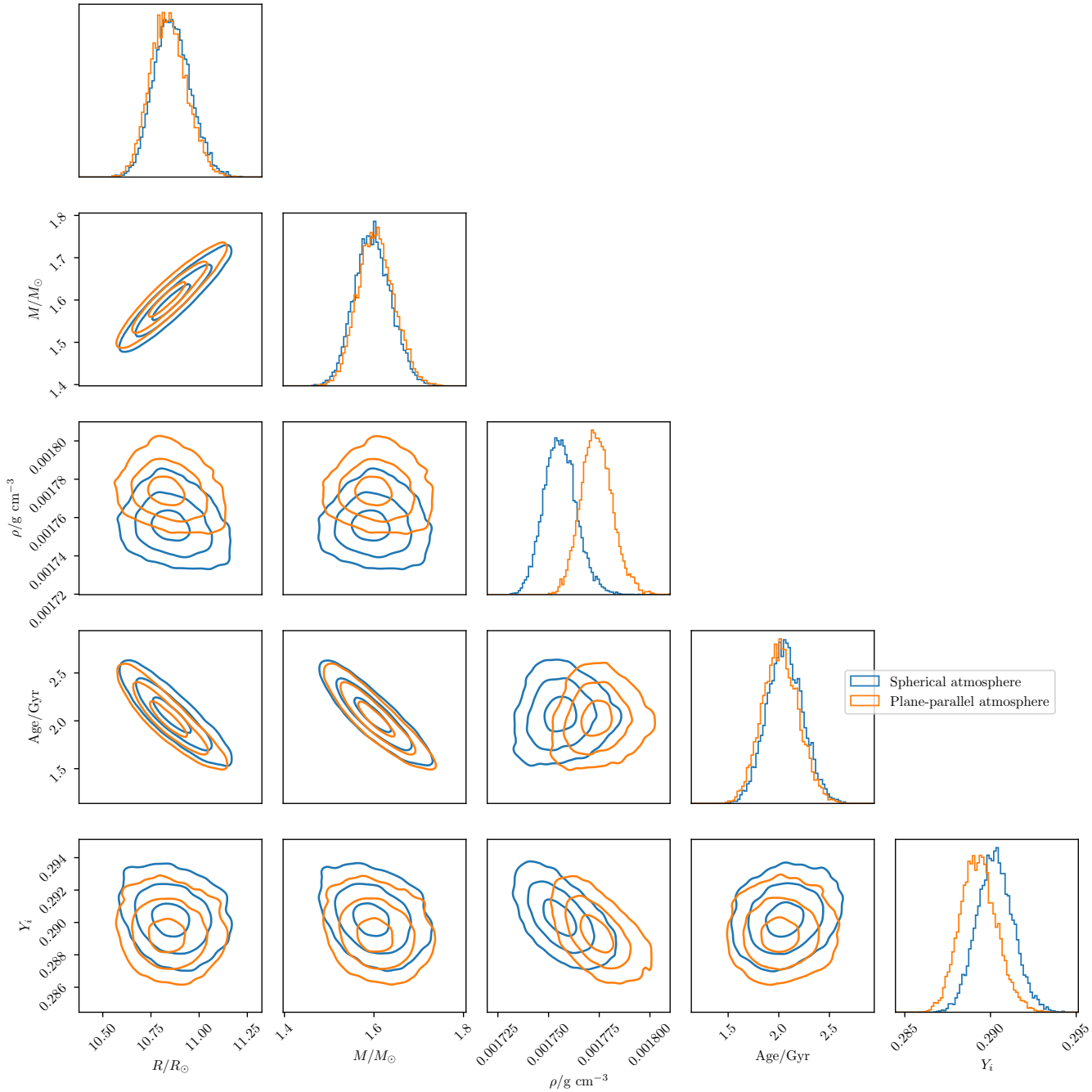

Figure 7. Joint posterior distribution of the stellar properties for KOI-3886, showing a comparison between each choice of physics in the underlying grids of evolutionary models.

Next, using the other pipeline (JO Pipeline; Sect. 4.2), we tested the impact of the model physics, namely, the atmospheric boundary condition, on the inferred stellar properties. Changing the atmospheric boundary condition is known to substantially modify the asteroseismic surface term — the differences in the mode frequencies between those of a star and a stellar model with identical interior structure, owing to modeling errors in the near-surface layers. Because these mode frequencies are measured far more precisely than the spectroscopic constraints, this surface term is typically assumed to dominate the systematic error when estimating stellar properties, if left uncorrected or corrected inappropriately. However, we have shown that even when using a seismic constraint designed to be independent of the near-surface structure of stellar models, inferences of stel-

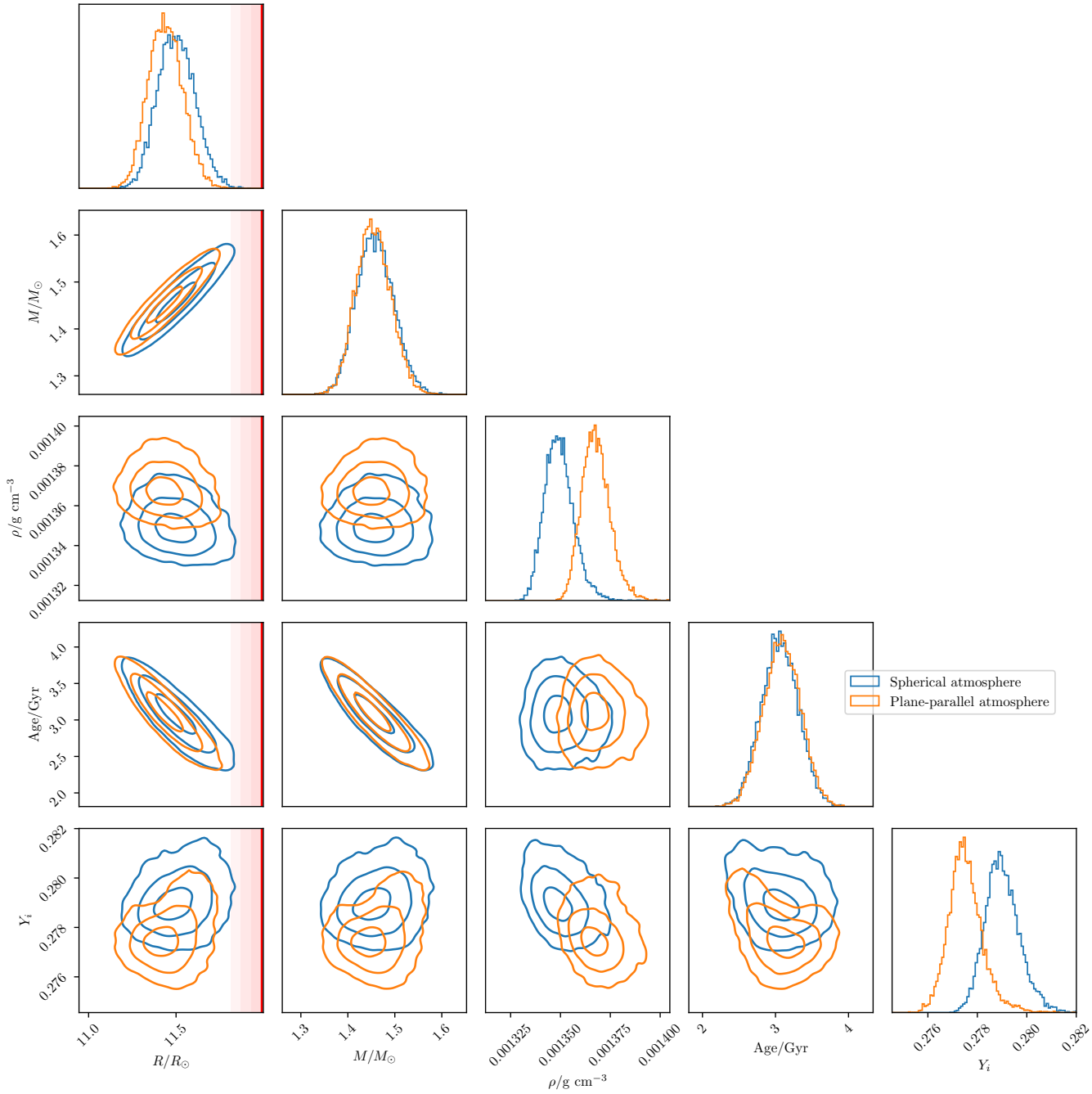

Figure 8. Joint posterior distribution of the stellar properties for ι Dra, showing a comparison between each choice of physics in the underlying grids of evolutionary models. The interferometric radius from Baines et al. (2011), as well as its associated uncertainty (1σ, 2σ, and 3σ), are depicted by the vertical line and shaded region, respectively.

lar properties are still significantly dependent on choices of atmospheric physics, as the spectroscopic properties of the models are also modified by changing the atmospheric boundary condition.

Facilities: *Kepler*, TESS, *Gaia*.

Software: KEPSEISMIC (https://archive.stsci.edu/prepds/kepseismic/), KADACS (García et al. 2011, 2014; Pires et al. 2015), DIAMONDS (Corsaro & De Ridder 2014), FAMED (Corsaro et al. 2020), MESA (Paxton et al. 2011, 2013, 2015, 2018), GYRE (Townsend & Teitler 2013).

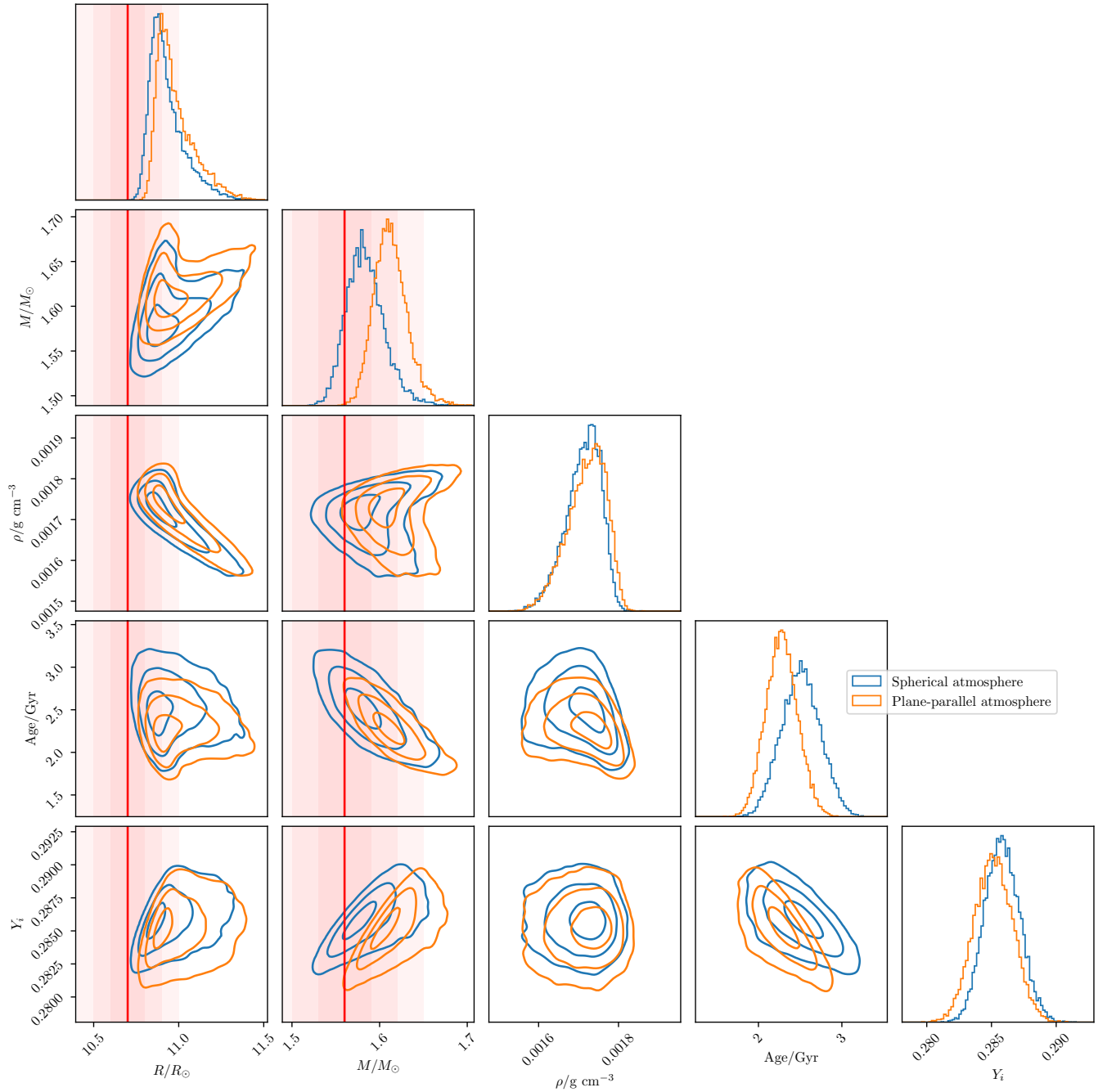

Figure 9. Joint posterior distribution of the stellar properties for KIC 8410637, showing a comparison between each choice of physics in the underlying grids of evolutionary models. The dynamical mass and radius from Frandsen et al. (2013), as well as their associated uncertainties (1σ, 2σ, and 3σ), are depicted by the vertical lines and shaded regions, respectively.

APPENDIX

Table A1. Extracted mode frequencies for KOI-3886.

$n_{\rm p}$	ℓ	Frequency (μHz)	1σ Uncertainty (μHz)	$p_{\rm det}$
6	0	32.629	0.047	1.000
6	1†,‡	34.846	0.021	0.996
6	1	34.971	0.031	1.000
6	2	36.434	0.065	1.000
6	1	36.806	0.012	0.996
7	0	37.080	0.036	1.000
7	1	39.011	0.044	1.000
7	1†,‡	39.302	0.042	—
7	2	40.813	0.057	1.000
8	0	41.408	0.065	—
8	1†,‡	43.830	0.041	—
8	2	45.452	0.057	—
9	0	46.049	0.057	—
9	1	47.833	0.038	0.999
9	1†,‡	48.444	0.045	—
9	2	50.045	0.070	—
10	0	50.604	0.063	—
10	1	52.573	0.030	1.000
10	1†,‡	53.030	0.041	—
10	1	54.068	0.021	1.000
10	1	54.397	0.035	1.000
10	2	54.703	0.046	—
11	0	55.233	0.068	—
11	1	56.196	0.078	0.994
11	1†,‡	57.715	0.061	—
11	1	58.213	0.033	1.000
11	2	59.482	0.061	1.000
11	1	59.705	0.026	1.000
12	0	59.830	0.025	1.000
12	1	61.922	0.006	0.993
12	1	62.155	0.025	0.998
12	1†,‡	62.370	0.011	1.000
12	1	62.509	0.015	0.997
12	2	64.136	0.100	1.000

† Manually selected p-like dipole modes (see Sect. 4.1.2).

‡ Manually selected p-like dipole modes (see Sect. 4.2.2).

A. FREQUENCY LISTS AND PEAK-BAGGING

REFERENCES

Aizenman, M., Smeyers, P., & Weigert, A. 1977, A&A, 58, 41

Asplund, M., Grevesse, N., Sauval, A. J., & Scott, P. 2009, Annual Review of Astronomy and Astrophysics, 47, 481, doi: 10.1146/annurev.astro.46.060407.145222

Table A2. Extracted mode frequencies for ι Dra.

$n_{\rm p}$	ℓ	Frequency (μHz)	1σ Uncertainty (μHz)	$p_{\rm det}$	List[a]
6	1	30.384	0.028	0.997	Min.
6	2	31.538	0.133	1.000	Min.
7	0	32.024	0.024	0.998	Min.
7	1[†,‡]	33.913	0.088	1.000	Min.
7	2	35.410	0.039	—	Min.
8	0	35.878	0.035	—	Min.
8	1[†,‡]	37.983	0.035	—	Min.
8	2	39.361	0.072	—	Min.
9	0	39.904	0.049	—	Min.
8	3	40.684	0.056	1.000	Max.
9	1	42.078	0.024	—	Max.
9	1	42.552	0.016	—	Min.
9	1	43.063	0.011	—	Max.
9	2	43.530	0.107	—	Min.
10	0	43.925	0.016	—	Max.
10	1[†,‡]	45.980	0.027	—	Min.
10	2	47.364	0.072	—	Min.
11	0	48.015	0.038	—	Min.
11	1[‡]	49.948	0.027	—	Min.
11	1	50.420	0.022	0.997	Max.
12	1	54.274	0.021	0.999	Min.
12	2	55.202	0.100	0.999	Max.
13	0	55.565	0.025	0.994	Max.

[a] 'Min.' = Belongs to Minimal List; 'Max.' = Belongs to Maximal List (but not to Minimal List). See Sect. 3.2 for a definition of both lists.

[†] Manually selected p-like dipole modes (see Sect. 4.1.2).

[‡] Manually selected p-like dipole modes (see Sect. 4.2.2).

Baines, E. K., McAlister, H. A., ten Brummelaar, T. A., et al. 2011, ApJ, 743, 130, doi: 10.1088/0004-637X/743/2/130

Ball, W. H., & Gizon, L. 2014, A&A, 568, A123, doi: 10.1051/0004-6361/201424325

Ball, W. H., Themeßl, N., & Hekker, S. 2018, MNRAS, 478, 4697, doi: 10.1093/mnras/sty1141

Ball, W. H., Chaplin, W. J., Nielsen, M. B., et al. 2020, MNRAS, 499, 6084, doi: 10.1093/mnras/staa3190

Basu, S., & Kinnane, A. 2018, ApJ, 869, 8, doi: 10.3847/1538-4357/aae922

Bedding, T. R., Mosser, B., Huber, D., et al. 2011, Nature, 471, 608, doi: 10.1038/nature09935

Borucki, W. J., Koch, D. G., Basri, G., et al. 2010, Science, 327, 977, doi: 10.1126/science.1185402

Bossini, D., Miglio, A., Salaris, M., et al. 2015, MNRAS, 453, 2290, doi: 10.1093/mnras/stv1738

Campante, T. L., Santos, N. C., & Monteiro, M. J. P. F. G., eds. 2018, Astrophysics and Space Science Proceedings, Vol. 49, Asteroseismology and Exoplanets: Listening to the Stars and Searching for New Worlds (Springer International Publishing), doi: 10.1007/978-3-319-59315-9

Campante, T. L., Handberg, R., Mathur, S., et al. 2011, A&A, 534, A6, doi: 10.1051/0004-6361/201116620

Campante, T. L., Schofield, M., Kuszlewicz, J. S., et al. 2016, ApJ, 830, 138, doi: 10.3847/0004-637X/830/2/138

Campante, T. L., Veras, D., North, T. S. H., et al. 2017, MNRAS, 469, 1360, doi: 10.1093/mnras/stx876

Campante, T. L., Corsaro, E., Lund, M. N., et al. 2019, ApJ, 885, 31, doi: 10.3847/1538-4357/ab44a8

Christensen-Dalsgaard, J., Silva Aguirre, V., Elsworth, Y., & Hekker, S. 2014, MNRAS, 445, 3685, doi: 10.1093/mnras/stu2007

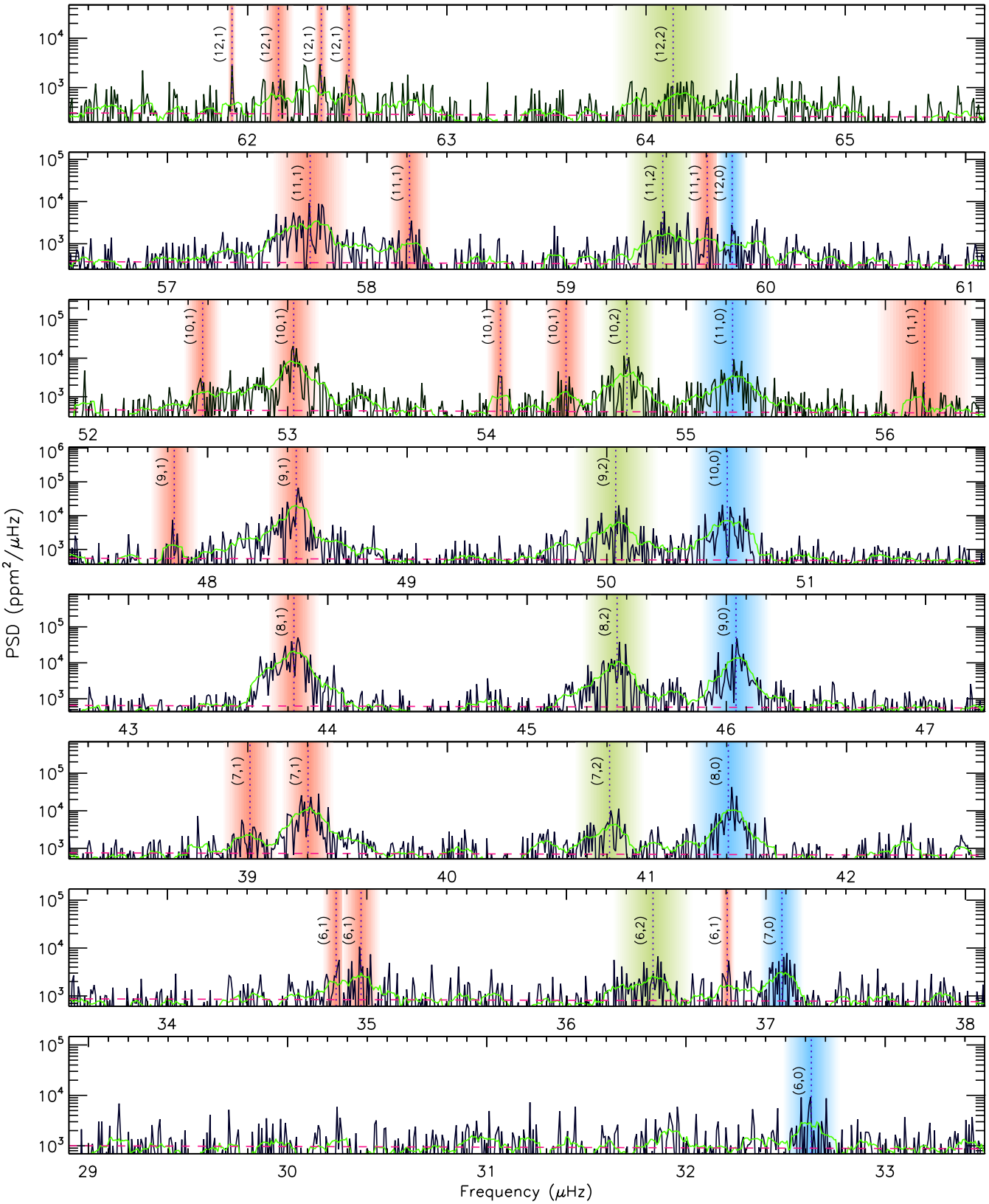

Figure A1. Stacked PSD of KOI-3886 showing the outcome of the peak-bagging process. The green curve is a smoothing of the power density by an amount equivalent to the average radial-mode linewidth found by FAMED. The sloping dashed line represents the local background. Extracted individual mode frequencies are tagged according to their pressure radial order ($n_{\rm p}$) and angular degree (ℓ), with color bands indicating their 3σ uncertainties.

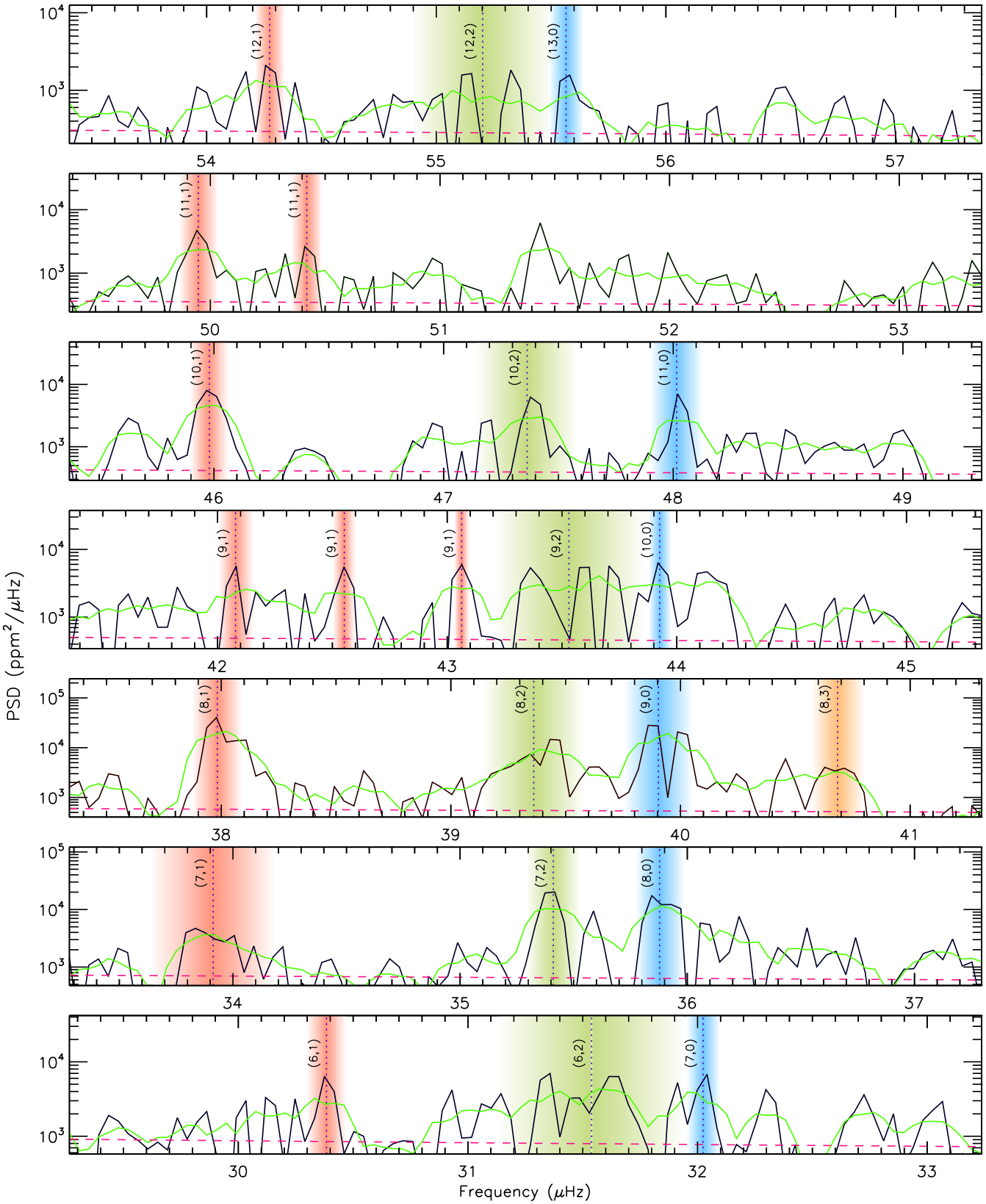

Figure A2. Stacked PSD of ι Dra showing the outcome of the peak-bagging process. Plot style similar to that of Fig. A1. The lower resolution of the TESS power spectrum of ι Dra is readily noticeable.

Christensen-Dalsgaard, J., Silva Aguirre, V., Cassisi, S., et al. 2020, A&A, 635, A165, doi: 10.1051/0004-6361/201936766

Compton, D. L., Bedding, T. R., Ball, W. H., et al. 2018, MNRAS, 479, 4416, doi: 10.1093/mnras/sty1632

Corsaro, E., & De Ridder, J. 2014, A&A, 571, A71, doi: 10.1051/0004-6361/201424181

Corsaro, E., McKeever, J. M., & Kuszlewicz, J. S. 2020, A&A, 640, A130, doi: 10.1051/0004-6361/202037930

Cunha, M. S., Roxburgh, I. W., Aguirre Børsen-Koch, V., et al. 2021, MNRAS, 508, 5864, doi: 10.1093/mnras/stab2886

Davies, G. R., Handberg, R., Miglio, A., et al. 2014, MNRAS, 445, L94, doi: 10.1093/mnrasl/slu143

Deheuvels, S., Ballot, J., Gehan, C., & Mosser, B. 2021, arXiv e-prints, arXiv:2108.11848. https://arxiv.org/abs/2108.11848

Elsworth, Y., Hekker, S., Basu, S., & Davies, G. R. 2017, MNRAS, 466, 3344, doi: 10.1093/mnras/stw3288

Ferguson, J. W., Alexander, D. R., Allard, F., et al. 2005, ApJ, 623, 585, doi: 10.1086/428642

Frandsen, S., Lehmann, H., Hekker, S., et al. 2013, A&A, 556, A138, doi: 10.1051/0004-6361/201321817

Frink, S., Mitchell, D. S., Quirrenbach, A., et al. 2002, ApJ, 576, 478, doi: 10.1086/341629

Gaia Collaboration, Brown, A. G. A., Vallenari, A., et al. 2021, A&A, 649, A1, doi: 10.1051/0004-6361/202039657

García, R. A., Hekker, S., Stello, D., et al. 2011, MNRAS, 414, L6, doi: 10.1111/j.1745-3933.2011.01042.x

García, R. A., Mathur, S., Pires, S., et al. 2014, A&A, 568, A10, doi: 10.1051/0004-6361/201323326

Gaulme, P., McKeever, J., Jackiewicz, J., et al. 2016, ApJ, 832, 121, doi: 10.3847/0004-637X/832/2/121

Grevesse, N., & Sauval, A. J. 1998, SSRv, 85, 161, doi: 10.1023/A:1005161325181

Grosjean, M., Dupret, M. A., Belkacem, K., et al. 2014, A&A, 572, A11, doi: 10.1051/0004-6361/201423827

Grunblatt, S. K., Huber, D., Gaidos, E., et al. 2019, AJ, 158, 227, doi: 10.3847/1538-3881/ab4c35

—. 2017, AJ, 154, 254, doi: 10.3847/1538-3881/aa932d

Grunblatt, S. K., Saunders, N., Sun, M., et al. 2022, AJ, 163, 120, doi: 10.3847/1538-3881/ac4972

Handberg, R., & Campante, T. L. 2011, A&A, 527, A56, doi: 10.1051/0004-6361/201015451

Herwig, F. 2000, A&A, 360, 952. https://arxiv.org/abs/astro-ph/0007139

Hill, M. L., Kane, S. R., Campante, T. L., et al. 2021, AJ, 162, 211, doi: 10.3847/1538-3881/ac1b31

Hon, M., Stello, D., & Yu, J. 2017, MNRAS, 469, 4578, doi: 10.1093/mnras/stx1174

—. 2018, MNRAS, 476, 3233, doi: 10.1093/mnras/sty483

Howell, S. B., Sobeck, C., Haas, M., et al. 2014, PASP, 126, 398, doi: 10.1086/676406

Huber, D., Stello, D., Bedding, T. R., et al. 2009, Communications in Asteroseismology, 160, 74. https://arxiv.org/abs/0910.2764

Huber, D., Carter, J. A., Barbieri, M., et al. 2013, Science, 342, 331, doi: 10.1126/science.1242066

Huber, D., Chaplin, W. J., Chontos, A., et al. 2019, AJ, 157, 245, doi: 10.3847/1538-3881/ab1488

Jiang, C., Bedding, T. R., Stassun, K. G., et al. 2020, ApJ, 896, 65, doi: 10.3847/1538-4357/ab8f29

Jofré, E., Petrucci, R., Saffe, C., et al. 2015, A&A, 574, A50, doi: 10.1051/0004-6361/201424474

Jørgensen, A. C. S., Montalbán, J., Miglio, A., et al. 2020, MNRAS, 495, 4965, doi: 10.1093/mnras/staa1480

Kallinger, T., Hekker, S., Mosser, B., et al. 2012, A&A, 541, A51, doi: 10.1051/0004-6361/201218854

Kane, S. R., Reffert, S., Henry, G. W., et al. 2010, ApJ, 720, 1644, doi: 10.1088/0004-637X/720/2/1644

Kane, S. R., Bean, J. L., Campante, T. L., et al. 2021, PASP, 133, 014402, doi: 10.1088/1538-3873/abc610

Khan, S., Hall, O. J., Miglio, A., et al. 2018, ApJ, 859, 156, doi: 10.3847/1538-4357/aabf90

Kuszlewicz, J. S., Hekker, S., & Bell, K. J. 2020, MNRAS, 497, 4843, doi: 10.1093/mnras/staa2155

Lagarde, N., Bossini, D., Miglio, A., Vrard, M., & Mosser, B. 2016, MNRAS, 457, L59, doi: 10.1093/mnrasl/slv201

Lenz, P., & Breger, M. 2005, Communications in Asteroseismology, 146, 53, doi: 10.1553/cia146s53

Li, T., Bedding, T. R., Christensen-Dalsgaard, J., et al. 2020, MNRAS, 495, 3431, doi: 10.1093/mnras/staa1350

Li, T., Bedding, T. R., Huber, D., et al. 2018, MNRAS, 475, 981, doi: 10.1093/mnras/stx3079

Li, T., Li, Y., Bi, S., et al. 2022, arXiv e-prints, arXiv:2201.09577. https://arxiv.org/abs/2201.09577

Lillo-Box, J., Barrado, D., Moya, A., et al. 2014, A&A, 562, A109, doi: 10.1051/0004-6361/201322001

Lillo-Box, J., Ribas, Á., Montesinos, B., et al. 2021, A&A, 653, A40, doi: 10.1051/0004-6361/202141158

Lomb, N. R. 1976, Ap&SS, 39, 447, doi: 10.1007/BF00648343

Lundkvist, M. S., Huber, D., Silva Aguirre, V., & Chaplin, W. J. 2018, Characterizing Host Stars Using Asteroseismology, ed. H. J. Deeg & J. A. Belmonte (Springer, Cham), 177, doi: 10.1007/978-3-319-55333-7_177

Magic, Z., Serenelli, A., Weiss, A., & Chaboyer, B. 2010, ApJ, 718, 1378, doi: 10.1088/0004-637X/718/2/1378

Malla, S. P., Stello, D., Huber, D., et al. 2020, MNRAS, 496, 5423, doi: 10.1093/mnras/staa1793

Marfil, E., Tabernero, H. M., Montes, D., et al. 2020, MNRAS, 492, 5470, doi: 10.1093/mnras/staa058

Mathur, S., García, R. A., Régulo, C., et al. 2010, A&A, 511, A46, doi: 10.1051/0004-6361/200913266
Miglio, A., Brogaard, K., Stello, D., et al. 2012, MNRAS, 419, 2077, doi: 10.1111/j.1365-2966.2011.19859.x
Mosser, B., Michel, E., Belkacem, K., et al. 2013, A&A, 550, A126, doi: 10.1051/0004-6361/201220435
Nielsen, M. B., Ball, W. H., Standing, M. R., et al. 2020, A&A, 641, A25, doi: 10.1051/0004-6361/202037461
Nsamba, B., Campante, T. L., Monteiro, M. J. P. F. G., et al. 2018, MNRAS, 477, 5052, doi: 10.1093/mnras/sty948
Ong, J. M. J., & Basu, S. 2020, ApJ, 898, 127, doi: 10.3847/1538-4357/ab9ffb
Ong, J. M. J., Basu, S., & McKeever, J. M. 2021a, ApJ, 906, 54, doi: 10.3847/1538-4357/abc7c1
Ong, J. M. J., Basu, S., & Roxburgh, I. W. 2021b, ApJ, 920, 8, doi: 10.3847/1538-4357/ac12ca
Paxton, B., Bildsten, L., Dotter, A., et al. 2011, The Astrophysical Journal Supplement Series, 192, 3, doi: 10.1088/0067-0049/192/1/3
Paxton, B., Cantiello, M., Arras, P., et al. 2013, The Astrophysical Journal Supplement Series, 208, 4, doi: 10.1088/0067-0049/208/1/4
Paxton, B., Marchant, P., Schwab, J., et al. 2015, The Astrophysical Journal Supplement Series, 220, 15, doi: 10.1088/0067-0049/220/1/15
Paxton, B., Schwab, J., Bauer, E. B., et al. 2018, The Astrophysical Journal Supplement Series, 234, 34, doi: 10.3847/1538-4365/aaa5a8
Pereira, F., Campante, T. L., Cunha, M. S., et al. 2019, MNRAS, 489, 5764, doi: 10.1093/mnras/stz2405
Pinçon, C., Takata, M., & Mosser, B. 2019, A&A, 626, A125, doi: 10.1051/0004-6361/201935327
Pires, S., Mathur, S., García, R. A., et al. 2015, A&A, 574, A18, doi: 10.1051/0004-6361/201322361
Reimers, D. 1975, Memoires of the Societe Royale des Sciences de Liege, 8, 369
Ricker, G. R., Winn, J. N., Vanderspek, R., et al. 2015, Journal of Astronomical Telescopes, Instruments, and Systems, 1, 014003, doi: 10.1117/1.JATIS.1.1.014003
Rogers, F. J., & Nayfonov, A. 2002, ApJ, 576, 1064, doi: 10.1086/341894
Rowe, J. F., Coughlin, J. L., Antoci, V., et al. 2015, ApJS, 217, 16, doi: 10.1088/0067-0049/217/1/16
Roxburgh, I. W. 2016, A&A, 585, A63, doi: 10.1051/0004-6361/201526593
Saunders, N., Grunblatt, S. K., Huber, D., et al. 2022, AJ, 163, 53, doi: 10.3847/1538-3881/ac38a1
Scargle, J. D. 1982, ApJ, 263, 835, doi: 10.1086/160554
Stello, D., Huber, D., Bedding, T. R., et al. 2013, ApJL, 765, L41, doi: 10.1088/2041-8205/765/2/L41
Stello, D., Saunders, N., Grunblatt, S., et al. 2022, MNRAS, 512, 1677, doi: 10.1093/mnras/stac414
Tayar, J., Claytor, Z. R., Huber, D., & van Saders, J. 2022, ApJ, 927, 31, doi: 10.3847/1538-4357/ac4bbc
Themeßl, N., Hekker, S., Southworth, J., et al. 2018, MNRAS, 478, 4669, doi: 10.1093/mnras/sty1113
Townsend, R. H. D., & Teitler, S. A. 2013, MNRAS, 435, 3406, doi: 10.1093/mnras/stt1533
Unno, W., Osaki, Y., Ando, H., Saio, H., & Shibahashi, H. 1989, Nonradial oscillations of stars (Tokyo: University of Tokyo Press)
Vrard, M., Kallinger, T., Mosser, B., et al. 2018, A&A, 616, A94, doi: 10.1051/0004-6361/201732477
Vrard, M., Mosser, B., & Samadi, R. 2016, A&A, 588, A87, doi: 10.1051/0004-6361/201527259
White, T. R., Huber, D., Mann, A. W., et al. 2018, MNRAS, 477, 4403, doi: 10.1093/mnras/sty898
Zechmeister, M., Reffert, S., Hatzes, A. P., Endl, M., & Quirrenbach, A. 2008, A&A, 491, 531, doi: 10.1051/0004-6361:200810405

This paper includes data collected by the *Kepler* and TESS missions. Funding for the *Kepler* and TESS missions is provided by the NASA Science Mission Directorate. This work was supported by Fundação para a Ciência e a Tecnologia (FCT) through research grants UIDB/04434/2020 and UIDP/04434/2020. This work was supported by FCT through national funds (PTDC/FIS-AST/30389/2017) and by FEDER through COMPETE2020 (POCI-01-0145-FEDER-030389). T.L.C. is supported by FCT in the form of a work contract (CEECIND/00476/2018). T.L. is supported by the European Research Council (ERC) under the European Union's Horizon 2020 research and innovation programme (CartographY; Grant Agreement no. 804752). J.M.J.O. was partially supported by NASA grant 80NSSC19K0374, awarded to Sarbani Basu. We thank the Yale Center for Research Computing for guidance and use of the research computing infrastructure. M.S.C. is supported by FCT in the form of a work contract (CEECIND/02619/2017). T.R.B. was supported by the Australian Research Council (DP210103119). S.N.B. and R.A.G. acknowledge support from the PLATO CNES grant. M.D. is supported by national funds through FCT in the form of a work contract. D.H. acknowledges support from the Alfred P. Sloan Foundation and the National Aeronautics and Space Administration (80NSSC19K0597, 80NSSC21K0652). C.J. is supported by a grant from the Max Planck Society to prepare for the scientific exploitation of the PLATO mission. C.K. acknowledges support from Erciyes University Scientific Research Projects Coordination Unit through grant DOSAP MAP-2020-9749. J.L.-B. acknowledges financial support received from the "la Caixa" Foundation under Marie Skłodowska-Curie fellowship with code LCF/BQ/PI20/11760023 and the Spanish State Research Agency (AEI) projects PID2019-107061GB-C61 and MDM-2017-0737. S.M. acknowledges support from the Spanish Ministry of Science and Innovation (MICINN) with the Ramón y Cajal fellowship no. RYC-2015-17697 and grant no. PID2019-107187GB-I00, and through AEI under the Severo Ochoa Centres of Excellence Programme 2020–2023 (CEX2019-000920-S). A.S. is supported by grants PID2019-108709GB-I00 of the Spanish MICINN and María de Maeztu CEX2020-001058-M.